2. Numerical SOC Models

Computers are useless. They can only give you answers.

Pablo Picasso

I do not fear computers. I fear the lack of them.

Isaac Asimov

Self-organized criticality (SOC) is the natural state into which a nonlinear dissipative system evolves into, without fine tuning of the initial conditions. Generally, some external forcing mechanism drives a system into criticality, where energy is dissipated sporadically in avalanche-like events. Such nonlinear dissipative systems are also called complex systems, which are composed of many interconnected parts that interact in a nonlinear way. Complex systems, such as the particles in a fluid that shows Brownian motion, have too many components to be described in terms of an n-body system with an equally large number of differential equations. So it is understandable that we first start with empirical computer simulations, which we call *numerical models*, to study the SOC state. In this chapter we exclusively describe such numerical models, in contrast to *analytical models* that will be developed in Chapter 3, based on approximations of the average behavior of some macroscopic physical parameters. The numerical models that have been used to study SOC behavior are mostly *cellular automaton* models, which essentially consist of an equi-spaced lattice grid and a set of mathematical rules to simulate a time-progressive interaction between next neighbors in the lattice. Hence, they are also called lattice-type simulations. There is no universal cellular automaton algorithm that works for every system in nature, but there is a rather large variety, each one adapted to capture the nonlinear dynamics of a particular phenomenon in nature. Thus we organize this chapter in the same order as Chapter 1, starting from small systems in laboratories out to the largest astrophysical systems in the universe. In addition to cellular automaton models, some other alternative numerical models have been used to study SOC behavior, such as mechanical systems (e.g., coupled pendulums or the block-slider model), n-body simulations (e.g., stellar dynamics), or percolation systems (e.g., solar active regions).

This chapter describes examples of numerical SOC simulations used in astrophysics (Sections 2.5–2.7), which essentially all were first inspired by non-astrophysical applications (Sections 2.1–2.4). Other generic reviews on numerical SOC models can also be found in Bak and Chen (1991), Bak and Paczuski (1995), Bak (1996), Jensen (1998), and Turcotte (1999).

2.1 SOC Simulations of Laboratory Experiments

As we have seen in Section 1.2, laboratory experiments with SOC behavior are difficult to carry out (especially with real sand or rice piles), so it is much easier to simulate these experiments with the computer. A few basic examples of computer models of laboratory experiments are coupled pendulums (Section 2.1.1), sandpiles (Section 2.1.2-3), lattice gases (Section 2.1.4), or coupled slider-block springs (Section 2.4.1), all representing idealized dissipative n-body systems that have a nonlinear coupling between next neighbor elements, from which the SOC behavior can be studied.

2.1.1 Coupled Pendulums

One of the prototypes of mechanical SOC models is a system of coupled oscillators, which mimic a complex system with many degrees of freedom. A relatively simple computer model was conceived by Tang et al. (1987), with a horizontal two-dimensional grid of pendulums that can rotate in a vertical plane and are mutually connected with the next neighbors with springs with force constant k (Fig. 2.1). The 2-D array of n pendulum balls of mass m is driven by a time-periodic square-wave force $F(t)$ and has the equation of motion

$$m\ddot{y} = -\gamma\dot{y}_j + k(y_{j+1} - 2y_j + y_{j-1}) - a\sin(2\pi y_j) + F, \qquad j = 1,2,...,n\ , \qquad (2.1.1)$$

where y_j is the position of the j-th pendulum ball, γ is the damping constant, and a is the amplitude of the potential. Tang et al. (1987) conducted computer simulations of this dissipative system and found novel patterns in the formation of metastable states. In further computer experiments of the group by Tang, Wiesenfeld, and Bak, energy was pumped into the system by random selection of pendulums that would perform a full initial rotation, which occasionally triggered adjacent pendulums to execute a full rotation (Fig. 2.1), similar to a domino effect. To make the system dissipative, a significant amount of friction was built in (with the damping constant γ). A typical experiment would involve 50×50 gridpoints (or $n = 2{,}500$ pendulums). Every random energy input triggered a different chain reaction of rotating pendulums, whose magnitude or size was counted by the number of pendulums that executed a full rotation during one chain reaction (or avalanche) event. Finally, the group of Tang, Wiesenfeld and Bak discovered that the size distribution $N(S)$ of avalanches as a function of the size S exhibited a powerlaw function in a log-log plot,

$$N(S) \propto S^{-\alpha}\ , \qquad (2.1.2)$$

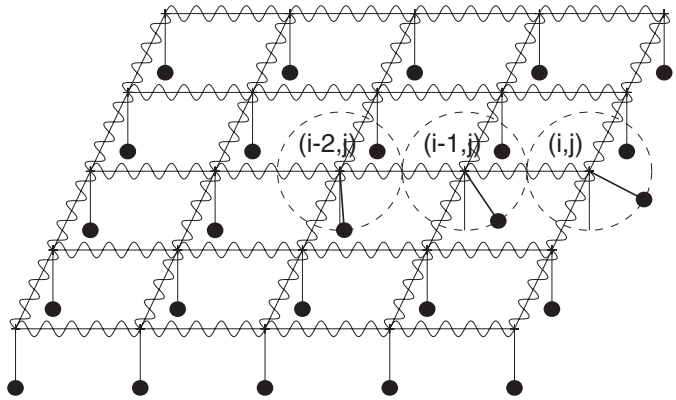

Fig. 2.1 System of coupled pendulums in a two-dimensional grid system as simulated by Tang et al. (1987). Each gridpoint has a pendulum that is coupled to its next neighbors with a spring. At the time shown, the pendulum at position (i, j) is excited and pulls the adjacent pendulums at positions $(i-1, j)$ and $(i-2, j)$ into the same direction through the coupling of the springs.

with a powerlaw slope of $\alpha \approx 1.1$ (see Fig. 11 in Bak 1996, p.47). At the upper end of the powerlaw distribution there is a cutoff given by the maximum number n of the pendulums contained in the system. This is one of the prototypes of nonlinear systems where the state of *self-organized criticality* (SOC) was discovered. The term "self-organizing" refers to the invariant endstate (with the same powerlaw slope) into which the system evolves, without fine tuning of the initial (random) energy input.

2.1.2 The Bak-Tang-Wiesenfeld 1-D Sandpile Model

The most famous paradigm of SOC models, introduced by Per Bak, is the sandpile. Sand grains are randomly dropped on a pile, which trigger avalanches of different sizes and durations. The system is dissipative because of the friction, which provides also the required instability threshold with many metastable states. The nonlinear dynamics comes in from the complicated collisional interactions at various scattering angles, speeds, kinetic, and gravitational energies of each sand grain involved in an avalanche. A complete analytical description of the kinematics of an n-body system that is involved in a sandpile avalanche would be prohibitively complex to solve, even when we include only the simplest mechanical forces occurring in collisions in a gravitational potential. The computer models of sandpiles are much simpler designed, reducing a sandpile just to a regular lattice grid with simple mathematical rules that mimic the interactions between neighbored pixels in a simplified way. In the simplest case, we envision just a one-dimensional sandpile, like the rice pile experiment between two parallel glass plates shown in Fig. 1.3. The 1-D sandpile model is also described in Bak et al. (1988), Bak (1996), and Jensen (1998).

The 1-D computer sandpile model resembles a histogram that has a number of h_i sand grains in each bin i (Fig. 2.2). The slope is defined by the difference $z_i = h_i - h_{i+1}$. The dynamics of sandpile avalanches is simply described by two operators: (a) adding a grain to

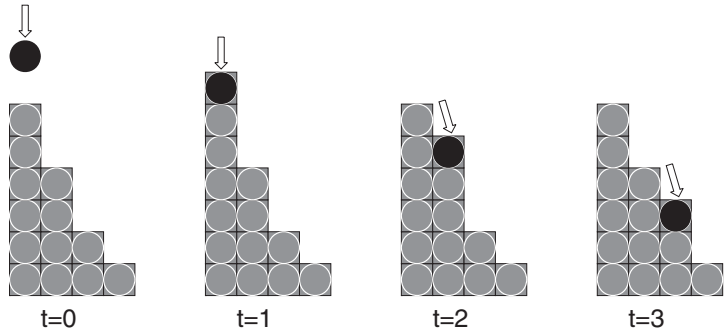

Fig. 2.2 Example of a 1-D Bak–Tang–Wiesenfeld sandpile. The dropped sand grain topples to the next lower level if the local slope $z_i = h_{i+1} - h_i = 2$ is steeper than a critical value of $z_c = 2$, i.e., when $z_i > z_c$. After the third time step the sandpile is stable again.

the pile, and (b) relaxing the slope of the pile wherever the local gradient exceeds a critical threshold for stability, i.e., $z_i > z_c$. In the simple example shown in Fig. 2.2 we have an initial state of $h_i, h_{i+1}, ..., h_{i+3} = [6,4,2,1]$. If we define a stable slope with a critical limit of $z_c = 2$, we see that the sandpile is stable, because the slope nowhere exceeds the critical limit. Now, we drop randomly a grain on the first bin, so that $h_i = 6+1 = 7$, which is unstable to the next bin, since $z_i = h_i - h_{i+1} = 7-4 = 3 > z_c$. Consequently, the unstable sand grain will topple into the next bin, i.e., $h_i = 7-1 = 6$ and $h_{i+1} = 4+1 = 5$, restoring the stable slope above, $z_i = h_{i+1} - h_i = 6-5 = 1$. However, this is unstable towards the next lower bin, since $z_{i+1} = h_{i+1} - h_{i+2} = 5-2 = 3 > z_c$. Consequently, the sand grain will topple into the next bin, i.e., $h_{i+2} = 5-1 = 4$ and $h_{i+3} = 2+1 = 3$, which is now stable everywhere with $h_i, h_{i+1}, ..., h_{i+3} = [6,4,3,1]$, and thus the avalanche stops. Thus, this little avalanche took two topplings. The number of sandgrains is conserved if we combine the previous sandpile plus the input. We note that the additional sandgrain falls on bin i and finally landed on bin $i+2$, while all the other bins stay the same. A system is said to be *"conservative"* when the number of sand grains is invariant during a redistribution rule. Even when sand grains are allowed to fall off the edge of a sandpile, the system can be conservative in the time average, if it balances the time-averaged input.

The dynamical behavior of this 1-D sandpile is easy to predict (Jensen 1998): Sand grains will pile up wherever the slope is less than critical, until the slope becomes critical everywhere. This critical state is also called *global attractor* (in nonlinear system dynamics) and is reached no matter where we start from initially. If we allow the system to exit the toppling sandgrains from the bin with the lowest number, the number of sand grains is conserved in the time average. Avalanches of different sizes are created by the random irregularities of local slopes that are slightly less (or equal) to the critical value. Therefore, the output of the system is highly fluctuating, even for a regular input rate, and thus the energy of the system is conserved in the time average only. The most remarkable property is the robustness of the endstate, which constitutes the concept of *self-organized criticality*.

2.1.3 The Bak–Tang–Wiesenfeld 2-D Sandpile Model

Since the world is not one-dimensional, the next logical step was to study SOC behavior in two dimensions, so our 2-D sandpile model is played now on a checker board, where each field has a 2-D position (i, j) in a cartesian coordinate system. The next-neighbor interactions are now extended to the 4 next neighbors at positions $(i-1, j)$, $(i+1, j)$, $(i, j-1)$, and $(i, j+1)$. One of the simplest SOC games that was initially studied had the simple setup of a critical threshold of $z_c = 4$ and the rule of a redistribution to the next 4 neighbors, whenever the local threshold was exceeded. So, there are two rules: (1) input of one grain at a random position, and (2) relaxation of four sand grains to the next 4 neighbors if a threshold of $z_c = 4$ is exceeded:

$$\begin{array}{ll} z(i,j) = z(i,j) + 1 & \text{initial input} \\ z(i,j) = z(i,j) - 4 & \text{if } z(i,j) \geq 4, \\ z(i \pm 1, j \pm 1) = z(i \pm 1, j \pm 1) + 1 & \end{array} \tag{2.1.3}$$

Such an algorithm is also called *cellular automaton*, because the dynamic evolution of a system is described by mathematical rules that enable "automated" steps, executed by interactions between the next neighbor cells in a (cellular) lattice grid.

Let us illustrate an avalanche in such a 2-D lattice sandpile model with an example given by Bak (1996; p.53), shown here in Fig. 2.3. Starting from an initially stable sandpile at time $t = 1$, a sand grain is dropped at position $z(3,3) = 4$, which makes it unstable and causes an avalanche. In the first toppling event between time $t = 2$ and $t = 3$, the unstable pixel changes its state $z(3,3) = 4 \mapsto 0$, while the 4 unstable sand grains get redistributed to the adjacent next neighbors at $z(2,3) = 2 \mapsto 3$, $z(3,2) = 3 \mapsto 4$, $z(3,4) = 2 \mapsto 3$, and $z(4,2) = 3 \mapsto 4$. Hence, we have two unstable pixels $z(4,3) = 4$ and $z(3,2) = 4$ at time $t = 3$ and the avalanche continues, until we reach a stable state at time $t = 9$ again. The envelope of all unstable sites that ever had an instability with $z(i, j) = 4$ entails a total of 8 pixel sites, which represents the area of the avalanche event. The time duration of the avalanche lasted 7 time steps, during which a total of 9 topplings occurred. In this example, a single sand grain is added at the beginning and further input is interrupted until the resulting avalanche comes to a halt, which is also called a *"stop-and-go"* sandpile, in contrast to a *running sandpile*, where the driver continues rregardless of simultaneous avalanching. In the former case, separate timescales control driving and avalanching.

In their seminal papers, Bak, Tang, and Wiesenfeld (1987, 1988) simulated such a cellular automaton algorithm for a 50×50 2-D lattice grid, as well as for a $20 \times 20 \times 20$ 3-D lattice grid. The 3-D generalization involves 8 nearest neighbors, and hence the rules are:

$$\begin{array}{ll} z(i,j,k) = z(i,j,k) + 1 & \text{initial input} \\ z(i,j,k) = z(i,j,k) - 8 & \text{if } z(i,j,k) \geq 8, \\ z(i \pm 1, j \pm 1, k \pm 1) = z(i \pm 1, j \pm 1, k \pm 1) + 1 & \end{array} \tag{2.1.4}$$

The avalanche size S was measured by the area of the clusters in the chain reaction of unstable pixels triggered by each single perturbation, and the duration T of an avalanche was measured by the number of toppling time steps that were needed until a stable configuration was reached. Bak et al. (1987, 1988) plotted then the distribution $N(S)$ of avalanche

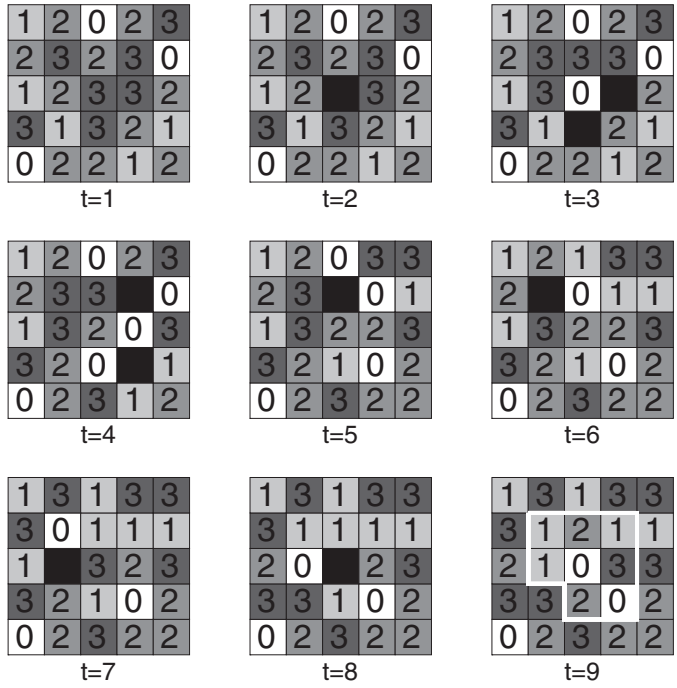

Fig. 2.3 Example of an avalanche in a 2-D Bak–Tang–Wiesenfeld sandpile. The initial state of the sandpile at time $t = 1$ is stable, since none of the states $z(i, j)$ exceeds the critical threshold $z_c = 4$. At time $t = 2$, a sand grain is dropped in the middle of the sandpile, which causes an avalanche of subsequent topplings. At times $t = 3$ and $t = 4$, two topplings occur in the same time step. At time $t = 9$, the sandpile becomes stable again and the total avalanche size is indicated with a white polygon, entailing 8 pixels (adapted from Bak 1996, p.53).

sizes S and durations T on a log-log scale and discovered the famous powerlaw distributions that have since become the hallmark of SOC. The pioneering results are shown in Fig. 2.4, where a powerlaw slope of $\alpha_S = 1.0$ was found for the avalanche sizes in the 2-D lattice over a range of more than two decades, and $\alpha_S = 1.37$ in the 3-D lattice. For the avalanche durations T, a powerlaw was fitted too,

$$N(T) \propto T^{-\alpha_T}, \tag{2.1.5}$$

yielding a slope of $\alpha_T \approx 0.43$ for the 2-D lattice, and $\alpha_T \approx 0.92$ for the 3-D lattice, respectively. All powerlaw distributions show a rollover cutoff at the upper end, which is a finite-size effect, indicating that the largest avalanche events are limited by the system size. These initial simulations were performed for a system with open boundaries $[z(1,y) = z(n+1,y) = z(x,1) = z(x,n-1) = 0]$, for two initial conditions: (a) far from equilibrium, and (b) far from a flat surface. Subsequent simulations were also performed for closed boundaries, but the results were identical for systems with open or closed boundaries, after the process was run for a while.

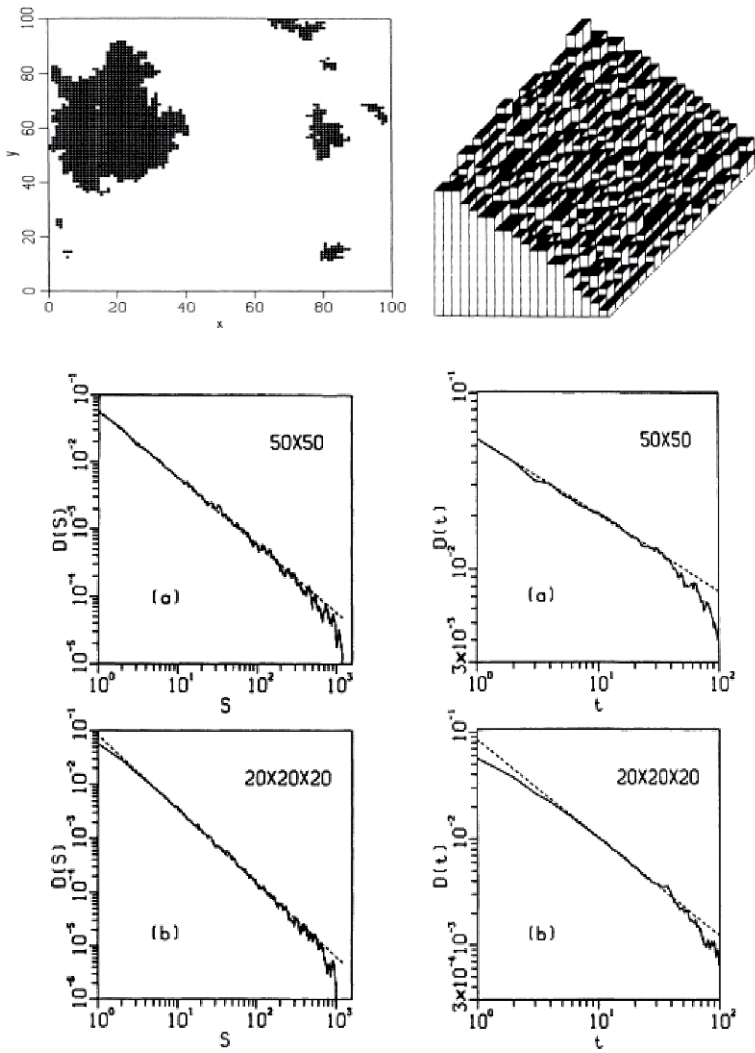

Fig. 2.4 Examples of a fragmented avalanche (top left) occurring in a 2-D (computer) sandpile (top right) and occurrence frequency distribution of avalanche cluster sizes (left panels) and avalanche durations (right panels) of the original BTW sandpile cellular automaton simulation. The simulations have been performed for a 50×50 2-D lattice (middle panels) and for a 20×20×20 3-D lattice grid (bottom panels). The powerlaw slopes are $\alpha_S = 1.0$ and $\alpha_T = 0.42$ for the 2-D grid (middle panels) and $\alpha_S = 1.37$ and $\alpha_T = 0.92$ for the 3-D grid. Reprinted from Bak, Tang, and Wiesenfeld (1987, 1988) with permission; Copyright by American Physical Society.

These initial results raise two interesting questions: (1) what is the physical interpretation of the powerlaw slopes α_S and α_T, and (2) how do the powerlaw slopes depend on the dimensionality (1-D, 2-D, 3-D) of the system? The value of the powerlaw index of time scales near unity, i.e., $\alpha_S \approx 1$, was brought in context of the $1/f$-noise (or white

noise), which scales with $P(\nu) \approx \nu^{-1}$. We will discuss the relationship between time scale distributions $N(T)$ and power spectra $P(\nu)$ in Section 4.8.

There is a large number of studies on the original BTW cellular automaton model, which either investigate the properties of the original BTW model or explore variants with modified rules. Some frequently quoted studies deal with: critical exponents and scaling relations (Tang and Bak 1988; Zhang 1989; Manna 1991a), two-state model of SOC (Manna 1991b), mean-field theory (Alstrom 1988; Christensen and Olami 1993; Zapperi et al. 1995; Vespignani and Zapperi 1997, 1998), preferred avalanche directions (Dhar and Ramaswamy 1989), invasion percolation (Roux and Guyon 1989), the *Abelian* property, i.e., the final state is invariant to the time order of the individual events (Dhar and Majumdar 1990; Majumdar and Dhar 1992; Dhar 1999), conservation laws and anisotropy (Grinstein et al. 1990), coexisting periodic attractors (Wiesenfeld et al. 1990), height correlations in sandpiles (Majumdar and Dhar 1991), avalanche dynamics at domain wall boundaries (Carlson et al. 1990), non-conservation in SOC models (Christensen et al. 1992; Socolar et al. 1993), renormalization group methods (Pietronero et al. 1994; Vespignani et al. 1995), the cutoff of the avalanche size distribution (Lise and Jensen 1996), the Landau–Ginzburg theory of SOC (Gil and Sornette 1996), emergent spatial structures (Tadic and Dhar 1997), critical values of driving field and dissipation (Dickman et al. 1998), and the universality of SOC models (Milshtein et al. 1998; Chessa et al. 1999). Reviews on BTW cellular automaton modeling and numerical simulations are given in Bak (1996), Jensen (1998), and Turcotte (1999).

2.1.4 The Lattice-Gas Model

The lattice-gas model is a particular cellular automaton model that has only a dual state per lattice point, either zero or one. One might think of the distribution of table tennis balls in a large egg carton (Fig. 2.5). If the tennis balls are shaken, they will fall back into the next hole, but only one ball can then occupy a hole. The lattice-gas model can be defined in multiple dimensions, but we consider a 2-D model in Fig. 2.5. Each cell contains either one or no particle, with no double occupancy. Neighboring particles repel each other by a unity force. At each timestep, the particles are redistributed according to a displacement vector that adds up the normalized forces,

$$\begin{aligned} x_{i',j'} &\mapsto Integer[x_{i,j} + F_x(i,j)/F] \\ y_{i',j'} &\mapsto Integer[y_{i,j} + F_y(i,j)/F] \end{aligned} \tag{2.1.6}$$

where $F = \sqrt{F_x^2 + F_y^2}$ is the total force, and the function $Integer[...]$ denotes the nearest integer number (i,j), because the positions (x_i, y_j) are defined in a discretized 2-D cartesian (lattice) grid. The rule (2.1.6) can only be applied if the new position $(x_{i',j'}, y_{i',j'})$ is empty. If two particles want to move to the same position, only the particle with the larger force wins and is moved, while the other stays at the old place. If two particles with equal force want to move to the same position, neither is moved. An example of a particle update during one time step is shown in Fig. 2.5. There are setups with closed boundaries, open boundaries, and periodic boundaries, which do not conserve the total number of particles

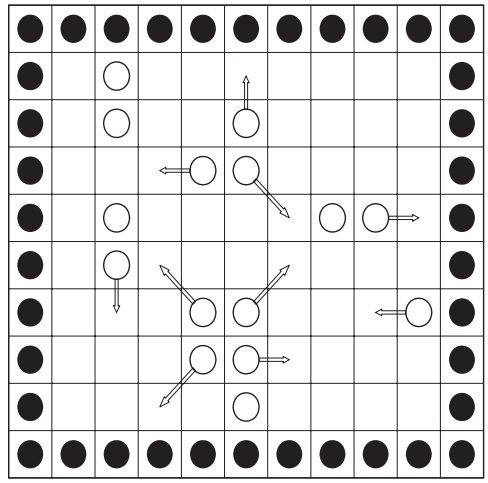

Fig. 2.5 Examples of particle updates in the lattice gas model. The boundaries are represented here with stationary particles (Jensen 1998).

inside the box. The fluctuations $n(t)$ of the total number of particles inside the box is of particular interest in the study of SOC.

Numerical simulations of the lattice-gas model are described in Jensen (1998) and have been studied by Jensen (1990), Fogedby et al. (1991), Andersen et al. (1991), and Fiig and Jensen (1993). The temporal fluctuations of the total number of particles $n(t)$ were found to follow a power spectrum $S(f)$ that is constant below a critical crossover frequency f_c, and a 1/f powerlaw above the crossover frequency,

$$S(f) \propto \begin{cases} \text{constant} & \text{if } f < f_{cr} \\ 1/f^{\gamma} & \text{if } f > f_{cr} \end{cases} , \tag{2.1.7}$$

where the powerlaw slope is $\gamma \approx 1$ and the crossover frequency scales as $f_{cr} \approx 1/L^2$ with the area L^2 of the lattice. Individual particles perform a random walk, as in a diffusion process. The lifetime T, defined by the number of time steps between entering and leaving of the box boundaries for an individual particle, was found to have a powerlaw distribution of

$$N(T) \approx T^{-\alpha_T} , \tag{2.1.8}$$

with $\alpha_T \approx 3/2$ for $T < T_{cr}$, where $T_{cr} \propto L^2$ scales with the area L^2 of the box. The lattice-gas system essentially exhibits SOC behavior, because it organizes itself scale-free with a $1/f$ power spectrum, except for finite-size effects at the upper end of time scales.

The lattice-gas model was found to exhibit the same SOC behavior as the flux noise experiment designed to study the onset of motion of vortices in a superconductor (Yeh and Kao 1984). The scale-invariant SOC behavior in the spatial and temporal scales in the motion of vortices in superconductors was demonstrated by Field et al. (1995).

2.2 SOC Simulations of Human Activities

2.2.1 Conway's Game of Life Model

Cellular automaton models, which are frequently used in numerical SOC models, have originally been devised by the British mathematician John Horton Conway in 1970 (Gardner 1970). One of the first applications was *Conway's Game of Life*, which was inspired by the problem of the mathematician John von Neumann, who tried to create a hypothetical machine (or robot) that could replicate itself, at least in a mathematical world with rectangular grids and mathematical rules.

We describe the original concept of Conway's Game of Life because it is the most basic prototype of a cellular automaton. We have an infinite two-dimensional orthogonal grid of square cells at our disposal, where each cell has the dual state of *live* or *dead* (like the binary memory plate of a computer). The game can be started by creating a particular initial state (of live or dead assignments to each cell), which is the only interaction of the player with the game, while the subsequent evolution is fully determined by mathematical rules. So, the player can just watch the evolution without further interaction or feedback. Each cell interacts with its 8 neighbors, sitting adjacent in horizontal, vertical, or diagonal direction. At each time step (or generation), the following 4 mathematical rules are applied (from *Wikipedia*):

1. Any live cell with fewer than 2 live neighbors dies (underpopulation).
2. Any live cell with more than 3 live neighbors dies (overcrowding).
3. Any live cell with 2 or 3 live neighbors lives on to the next generation.
4. Any dead cell with exactly 3 live neighbors becomes a live cell.

The game can evolve into myriads of unexpected interesting patterns (called "gliders", "blinkers", "F-pentomino" "boat", "pulsar", "diehard", "acorn", and so forth; see examples in Fig. 2.6), similar to a chess game, except that the game evolves automatically without any players interaction. The original motivation of Conway's Game of Life was the study of initial configurations that lead to population growth, extinction, oscillatory, or stable situations. Numerical simulations revealed that specific patterns emerged recurrently, as

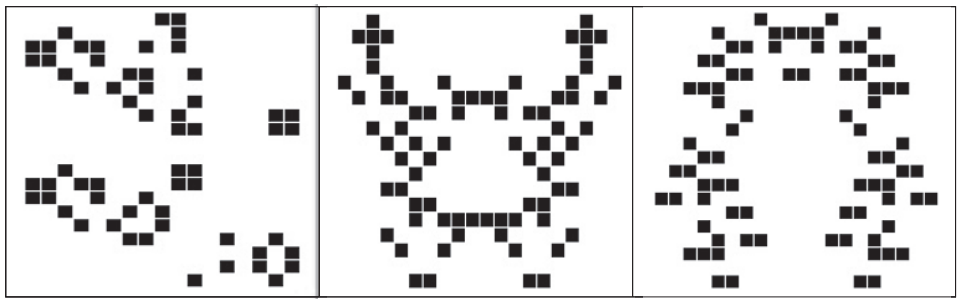

Fig. 2.6 Examples of "glider" structures occurring in Conway's Game of Life. Note the fractal structure of these replicating structures (credit: Eppstein).

well as an infinite variety and richness of self-organizing structures that were thought to mimic aspects of the emergence of complexity in nature.

Bak, Chen, and Creutz (1989) wondered whether the Game of Life was in a critical state with SOC behavior. They simulated a game until it came to a static situation (ending up with static structures and simple oscillatory "blinkers"), and defined this way a time duration T from the number of time steps it took to become static, and a size S from the number of births and deaths occurring during one game, which represents an avalanche event in the SOC terminology. The game was repeated by just changing one random cell, like adding a sandgrain to a stable sandpile, and they sampled the next avalanche, continuing the game ad infinitum. The statistical outcome was indeed a powerlaw distribution with a slope of $\alpha_S = 1.3$ for the size distribution $N(s/L)$, i.e., normalized by the system size L (Bak 1996). A computer simulation of 40,000 games (avalanche events) on a 100×100 lattice grid exhibited powerlaw size distributions with slopes of $\alpha_S = 1.4$ for spatial scales and $\alpha_T = 1.6$ for temporal scales (Bak, Chen, and Creutz 1989), but a rollover at the upper cutoff was found that was interpreted as finite-size effect. This finding of finite-size effects at the upper cutoff was later confirmed with 1024×1024 lattice grid simulations (Alstrom and Leao 1994).

2.2.2 Traffic Jam Simulations

We alluded to the SOC behavior of traffic jams in Section 1.3. Although traffic seems to be a highly complex system with many different vehicles and driver individuals, the basic dynamics of traffic jams can be simulated and understood in a relatively simple way. Nagel and Paczuski (1995) used the following model. The traffic system is reduced to a single-lane freeway, represented by a one-dimensional array of length L. The spatial position of the highway is discretized to x_i, $i = 1,...,n$, with $x_n = L$. In each position x_i there are $v_{max}+2$ states, either it is empty (with no car) or occupied (with a car) with an (integer) velocity $v_i = 0,...,v_{max}$, where they choose $v_{max} = 5$ in their simulations. A basic (cellular automaton) rule is that car movements occur "crash free". To reinforce this rule, the velocity of each car has to be adjusted to the distance of the car in the front, which is defined by the number of pixels n_{gap} between two car-occupied pixels. The detailed mathematical rules for crash-free traffic in this system are:

1. A vehicle is stationary when it travels at maximum velocity v_{max} and has free headway, $n_{gap} \geq v_{max}$, just maintaining its velocity, and is updated by $x(t_{i+1}) = x(t_i) + v_{max}\Delta t$.
2. If a vehicle is not stationary, it is jammed, in which case two possible rules apply:
   (a) *Acceleration of free vehicles:* A vehicle with spacing $n_{gap} = v$ maintains its velocity, while a vehicle with spacing $n_{gap} \geq v+1$ accelerates to $v(t_{i+1}) = v(t_i)+1$ with a probability of $1/2$.
   (b) *Deceleration due to other cars:* Each vehicle with an "unsafe" gap of $n_{gap} \leq v_1$ has to slow down to $v(t_{i+1}) = v(t_i)-1$ in subsequent time steps until it regains an ideally safe distance of $v = n_{gap}$. However, the slow-down manoeuvre is a bit randomized with a probability of $1/2$ to end up in a slightly too small interval $v = n_{gap}+1$ (for tail-gaters) or $v = n_{gap}-1$ (for very cautious drivers).

3. *Movement:* In each time step Δt, each vehicle moves to position $x(t_{i+1}) = x(t_i) + v\Delta t$, excluding backward motions ($v \geq 0$).

The outcome of such a one-dimensional traffic simulation is shown in Fig. 2.7, where the spatial position is the horizontal direction and time is progressing downward in vertical direction. Free vehicles with constant speed move along diagonals from top left to bottom right, while jams are visible as concentrations of slower velocities (steeper diagonals) that propagate backward on the street, and eventually dissolve. In SOC parlance, every local jam is called an "avalanche", and the lifetime T of an avalanche is defined by the number of time steps it takes until the number of jammed cars is zero. Furthermore, the spatial extent w of a jam, the number of jammed vehicles n, and the overall space-time size $s \approx nT$ (mass) of the jam can be measured. Fig. 2.8 shows the probability distribution $P(T)$ of jam lifetimes, which in this numerical simulation yielded a perfect powerlaw distribution with a powerlaw slope of $\alpha_T = 1.50 \pm 0.01$ over six orders of magnitude, limited by the maximum time span of the simulation at $t = 10^6$,

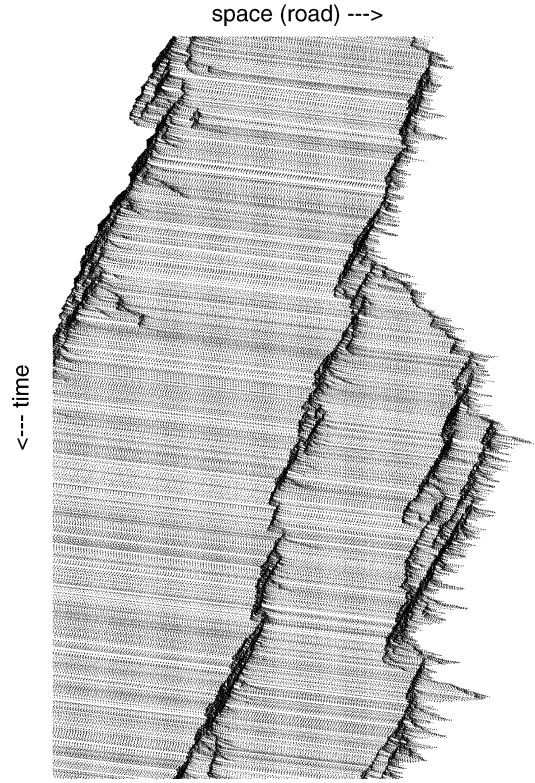

Fig. 2.7 Traffic jam simulations of a 1-D model (with space coordinate in horizontal direction and time running down in vertical direction) showing laminar flows (undisturbed diagonal car traces) and congestions (dark ridges). Reprinted from Nagel and Paczuski (1995) with permission; Copyright by American Physical Society.

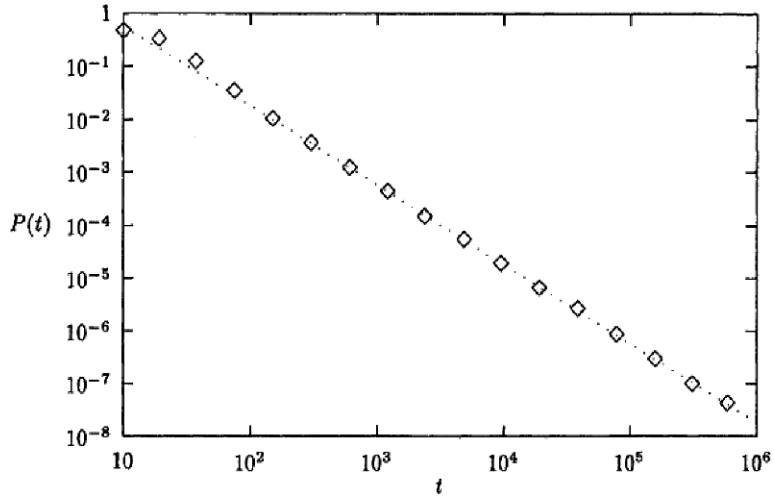

Fig. 2.8 Lifetime distribution $P(T)$ of emergent traffic jams in the outflow region, averaged over more than 65,000 jams. A powerlaw slope of $\alpha_T = 1.50 \pm 0.01$ is found (Nagel and Paczuski 1995).

$$P(T) \propto T^{-\alpha_T} \ , \quad \alpha_T = 1.50 \pm 0.01 \ . \tag{2.2.1}$$

It is a quite surprising result that complex traffic behavior can be nailed down by a single number α_T in the framework of the SOC concept. Is this numerical value of $\alpha_T = 3/2$ a magic number with a deeper physical meaning? Nagel and Paczuski (1995) provide a simple analytical model that explains this value in terms of one-dimensional random walk. Since a random walk or diffusion process is a well-understood concept, we outline the analytical connection between diffusion and SOC behavior here, because it gives us a deeper physical insight for this particular SOC system.

The probability distribution $P(n,t)$ for the number n of cars in the jam at time t can be described by the following rate equation,

$$P(n,t+1) = (1 - r_{in} - r_{out})P(n,t) + r_{in}P(n-1,t) + r_{out}P(n+1,t) \ , \tag{2.2.2}$$

where the rates r_{in} and r_{out} represent empirical quantities that depend on the car densities behind and in front of the jam. For large numbers n the rate equation (2.2.2) transforms into the differential equation,

$$\frac{\partial P}{\partial t} = (r_{out} - r_{in})\frac{\partial P}{\partial n} + \frac{r_{out} + r_{in}}{2}\frac{\partial^2 P}{\partial n^2} \ , \tag{2.2.3}$$

For sake of simplicity we consider the equilibrium case when the rate of cars entering the jam equals the cars leaving the jam, i.e., $r = r_{in} = r_{out}$, in which case we obtain the one-dimensional diffusion equation,

$$\frac{\partial P}{\partial t} = r\frac{\partial^2 P}{\partial n^2} \ . \tag{2.2.4}$$

If we plug in the observed probability of lifetimes, $P(t) \propto t^{-3/2}$, into the left side, i.e., $\partial P/\partial t \propto t^{-5/2}$, and use the solution of a diffusion process for one-dimensional random walk,

$$n \propto t^{1/2} \,, \tag{2.2.5}$$

we infer a probability $P(n)$ for the number n of cars involved in a jam,

$$P(n) \propto (t^{1/2})^{-3/2} = n^{-3} \,, \tag{2.2.6}$$

which fulfills the diffusion equation (2.2.4), since $\partial^2 P/\partial n^2 \propto n^{-5} \propto t^{-5/2}$. Thus, the evolution of a traffic jam simulation behaves like a one-dimensional diffusion process and explains the observed powerlaw distribution of $P(T) \propto T^{-3/2}$ of jam lifetimes. Remarkably, the simple diffusion process explains not only the powerlaw behavior of this SOC system, but also the value of the powerlaw slope for lifetimes. Note, that the same powerlaw index of $\alpha_T = 3/2$ was also found for lattice gas models (Section 2.1.3), but is different for sand avalanches in the BWT model (Section 2.1.2), where also the dimensionality of the system plays a role.

Some first pioneering Monte-Carlo simulations of 1-D traffic jams that mimic the transition from laminar (uncongested) traffic flow to (congested) start–stop-waves with increasing car density were performed by Nagel and Schreckenberg (1992) and Nagatani (1995a,e,f). Deterministic 1-D traffic jam models with continuous positions and velocities showed that SOC behavior is driven by the slowest car (Nagel and Herrmann 1993). Further SOC studies on traffic jams involved temporary stopping of cars (Nagatani 1995d), entering and exiting of cars on highway ramps (Nagatani 1995b), and 2-D cellular automaton models (with many parallel highway lanes) to avoid jam driving (Nagatani 1995c). A major conclusion of traffic jam simulations is that the critical state of SOC behavior occurs at the maximum throughput rate. Thus, if we want to make our highways most efficient and achieve the highest throughput rate, we have to expect traffic jams at the critical state of SOC. So, we cannot have maximum throughput without traffic jams! The throughput rate is controlled today by metering lights at the entering ramps of some highways, for instance in California.

2.2.3 Financial Market Simulations

One of the first SOC concepts applied to the financial market is the BCSW model of fluctuations in aggregate production (Bak, Chen, Scheinkman, and Woodford 1993). It is a variation of the 2-D BTW sandpile model (Bak, Tang, and Wiesenfeld 1987) in which sites on the lattice represent firms, while the interactions between next-neighbor lattice points are sales and purchases of products. An avalanche starts with the input of a product on the market, which triggers a chain reaction of sales and purchases. High prices produce small avalanches, while low prices can create large avalanches. The SOC behavior explains the large fluctuations in aggregate production.

A related concept is the multiple-strategy agent-based model. For instance, one such model envisions a self-organized network of competing Boolean agents who compete on the market based on actions and information obtained from a small group of other agents

(Paczuski et al. 2000). The agents play a competitive game that rewards those in the minority. Computer simulations of this model show that the network evolves to a stationary but intermittent state where random mutation of the worst strategy can change the behavior of the entire network.

SOC modeling and simulations of the financial market is comprehensively summarized in the review entitled "Financial physics" by Feigenbaum (2003), entailing the BCSW sandpile model (Bak et al. 1993), the percolation model of Cont and Bouchard (2000), multiple-strategy agent-based models (e.g., Paczuski et al. 2000), the minority game model (Challet and Zhang 1997), and log-periodic precursors to financial crashes (Feigenbaum and Freund 1996; Sornette and Johansen 1997). SOC simulations of the financial market may be able to explain some universal scalings that have been observed for widely different economies and different time epochs: (i) the fluctuation of price changes of any stock market is characterized by a probability density function that is a simple power law with an exponent $\alpha = 3$ extending over 8 orders of magnitude (on the y-axis), and (ii) for a wide range of economic organizations, the size of organizations is inversely correlated to the fluctuations in size with an exponent of $\beta \approx 0.2$ (Stanley et al. 2002).

2.3 SOC Simulations in Biophysics

2.3.1 The Punctuated Equilibrium (Bak–Sneppen Model)

Biological evolution is not a gradual process. Genetic mutations that lead to the origin of new species, or natural disasters that lead to mass extinctions, happen very intermittently, separated by long quiescent periods of near-equilibrium. This mixed state of near-equilibrium and rare loss-of-equilibrium events is called the theory of punctuated equilibrium. A numerical model with punctuated equilibrium and criticality applied to evolution was developed by Bak and Sneppen (1993). It is a cellular automaton model with a one-dimensional set of n sites, where each site represents a species and its fitness ρ_i is characterized with a random number between zero and unity, i.e. $0 \leq \rho_i \leq 1$. At each time step, the site with the smallest value of ρ_i is replaced by a new random value from the range $0 \leq \rho_i \leq 1$, which corresponds to a random mutation of the least-fit species (or dissipation of the least-fit organism in a food chain). After many steps, a quasi-stationary state is established where all values end up in a restricted range of $\rho_c \leq \rho_i \leq 1$, where a critical value of $\rho_c = 0.6670$ is found. This state corresponds to a near-equilibrium situation where each species has a minimal fitness of ρ_c, essentially capturing Charles Darwin's notion of the evolution theory where only the fittest species survive. Continuing the random mutations, either the equilibrium is maintained if a new assigned state is larger than the critical value, $\rho_i \geq \rho_c$, or an avalanche is started when $\rho_i < \rho_c$. Thus, an avalanche of evolutionary changes propagates to the adjacent sites, until a new equilibrium is obtained with all fitness values $\rho_i \geq \rho_c$. Counting the number of species that temporarily have a fitness value of $\rho_i < \rho_c$ defines the size of a (mutation) avalanche. Bak and Sneppen (1993) found a powerlaw frequency distribution for the avalanche sizes with a slope of $\alpha \approx 1$ for a 1-D model, and $\alpha \approx 1.26$ for a 2-D model. Tracking a single species i, there are long time periods when the fitness parameter $\rho_i(t)$ does not change, but once it or its

next neighbor becomes the species with the lowest fitness, it is part of a chain-reaction of mutations until the whole neighborhood is restored into quasi-equilibrium. Consequently, a plot of the number of mutations as a function of time has the appearance of a sequence of irregular step functions (i.e., a "Devil's staircase"), which is the hallmark of punctuated equilibrium theory (Bak and Paczuski 1995). A visualization of the "fractal evolution" of the Bak–Sneppen model is shown in Fig. 2.9. The time intervals of quasi-equilibrium can be considered as lifetimes of a species, while the "punctuations" or episodes of mutations represent a transition, equivalent to an extinction and replacement of a species. Such a simulated evolution of extinctions could mimic the observed powerlaw distribution of some 19,000 species extinctions observed in fossil history by Raup (1986) and Sepkoski (1993), see Fig. 1.6 and discussions in Bak and Paczuski (1995), Sneppen et al. (1995), and Bak (1996).

This simple cellular automaton model for evolution could also be treated analytically in terms of mean field theory. In a one-dimensional model, the dynamics can be described in terms of a "repetitious random walker" and anomalous diffusion diffusion with exponent 0.4 (Flyvbjerg et al. 1993). The distribution of avalanche durations (or co-evolutionary mutations) has a mean field exponent of $\alpha_T = 3/2$ (de Boer et al. 1994, 1995). A conjecture

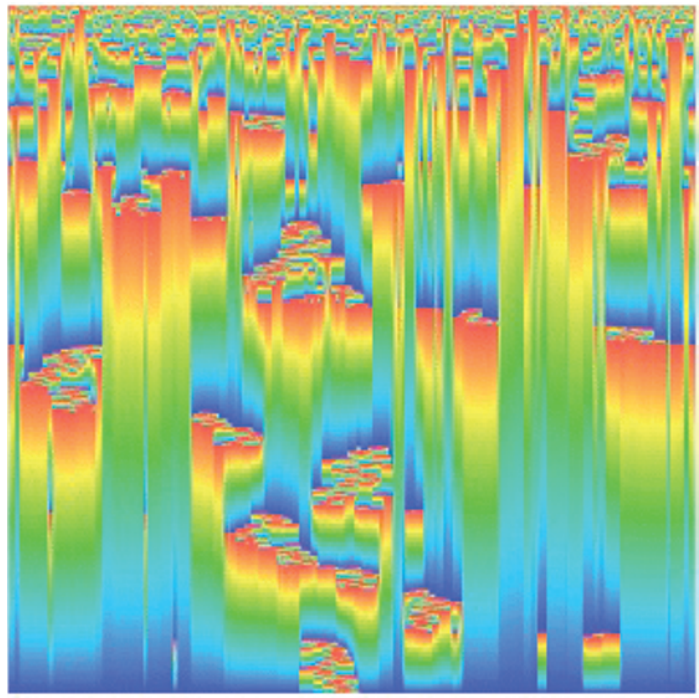

Fig. 2.9 Sample of the Bak–Sneppen model evolution. The population status (or species number) is shown on the *x*-axis and the history (or time) is on the *y*-axis from top to bottom. Each "floating iceberg" structure (visualized with a shading along the *z*-axis) represents a population episode of evolution or extinction (credit: Claudi Rocchini).

that the same model applies to Reggeon field theory (Grassberger and de la Torre 1979) in high-energy particle physics was made by Paczuski et al. (1994), and Ray and Jan (1994), and the analytical derivation in terms of the "gap equation" and the "gamma equation" is discussed in Bak and Paczuski (1995). Scaling laws of SOC powerlaw coefficients and power spectra are studied in Maslov et al. (1994), Paczuski et al. (1996), Böttcher and Paczuski (1996, 1997), and Sole and Manrubia (1996). Reviews of the Bak–Sneppen SOC model applied to biological evolution can also be found in Turcotte (1999) and Sole et al. (1999). The mean field theory applied to the Bak–Sneppen model is summarized in Jensen (1998).

2.4 SOC Simulations in Geophysics

2.4.1 Slider-Block Spring Model

The slider-block spring model (Fig. 2.10) is a mechanical model that was especially designed to mimic the forces between tectonic plates in the Earth's crust, where each stick-and-slip motion is manifested as an earthquake. Alternatively, one can also think of pulling sandpaper across a carpet. This mechanical model consists of two plates and a set of mass elements that all are elastically coupled between neighboring elements, similar to the coupled pendulums described in Section 2.1. All elements experience the same driving force from the upper driver plate, but the individual elements, which are elastically coupled to both the next neighbors as well as to the driver plate, execute a stick-and-slip motion due to the friction on the rough surface. A block moves when the pulling force exceeds the static friction F_s. Once a block moves, it experiences a smaller amount of friction (i.e., dynamic friction, with $F_d < F_s$) than in rest. The elastic coupling can trigger a number of neighbored blocks to slip in a chain reaction, which produces an avalanche, and thus SOC behavior is expected in a similar way as for the coupled pendulums or sandpiles. This type of slider-block spring model has been originally introduced by Burridge and Knopoff (1967).

The mechanical force acting on a block in the slider-block spring model is composed of the driver (leaf) spring constant k_p and the connector spring constants k_c (see Fig. 2.10),

$$F_i(t) = m\frac{d^2x_{i,j}}{dt^2} + k_p\, x_{i,j} + k_c(x_{i+1,j} + x_{i-1,j} + x_{i,j+1} + x_{i,j-1} - 4x_{i,j}) = F_d \ , \qquad (2.4.1)$$

where $x_{i,j}$ is the position of block (i, j), t is the time, and F_d is the dynamic frictional force during motion. When the block is at rest, we have the inequality condition,

$$k_p x_{i,j} + k_c(x_{i+1,j} + x_{i-1,j} + x_{i,j+1} + x_{i,j-1} - 4x_{i,j}) < F_s \ , \qquad (2.4.2)$$

where F_s is the static resisting force. The dynamical behavior of the system can be characterized by the free parameters of the ratio of the static to dynamic friction (F_d) and the stiffness of the system ($q_k = k_c/k_p$). For soft systems, $q_k \mapsto 0$, the blocks exhibit stick-and-slip behavior independently, while stiff systems, $q_k \mapsto \infty$ show more coherent motions as a

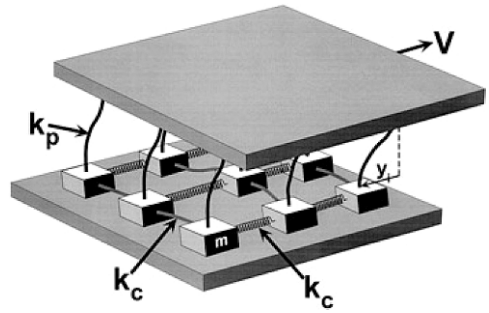

Fig. 2.10 The slider-block model consists of an array of blocks, each with mass m, which are pulled across a surface by a driver plate at a constant velocity v. Each block is coupled to the adjacent blocks with either leaf or coil springs (with spring constant k_c), and to the driver plate with leaf springs (with spring constant k_p) (Turcotte 1999). (Reprinted with permission of the American Physical Society)

whole. Stiff systems produce an over-abundance of coherent large-scale slips (with peaks at the high end of the occurrence frequency distribution), while soft systems exhibit powerlaws for small events, but a lack of large events (Huang et al. 1992). Typical powerlaw distributions with a slope of $\alpha \approx 1.0$–1.3 are found for such systems (Turcotte 1999).

Early computer simulations with 2,000 slider blocks revealed a powerlaw distribution for the occurrence frequency of events as a function of the number of blocks that slip (event size), and thus evidence for SOC behavior was found (Otsuka 1972). Simulations of a 1-D chain of 400 blocks using a velocity-weakening (nonlinear) friction law also exhibited chaotic behavior and powerlaw distributions of slip avalanches, which are characteristic of SOC behavior (Carlson and Langer 1989a,b). Using a cellular-automaton model of threshold elements, instead of solving the differential equations (2.4.1–2.4.2), greatly simplified the calculations (Nakanishi 1990, 1991; Brown et al. 1991). A large number of studies on the slider-block spring model have been conducted and variants of it have been modeled and simulated, such as the following frequently quoted studies: Smalley et al. (1985), Sornette and Sornette (1989), Rundle and Klein (1989), Carlson (1991a,b), Carlson et al. (1991), Feder and Feder (1991), the Olami–Feder–Christensen model (Olami et al. 1992), Christensen and Olami (1992a,b), Shaw et al. (1992), Cowie et al. (1993), de Sousa Vieira et al. (1993), Grassberger (1994), Shaw (1995), or Middleton and Tang (1995). The slider-block spring model is the primary basis for associating earthquakes with SOC (Turcotte 1999), but alternative models also have been proposed, such as the crack propagation model (Chen et al. 1991) and interface depinning (Paczuski and Böttcher 1996; Fisher et al. 1997). Reviews on the slider-block spring model can be found in Carlson et al. (1994), Bak (1996), Turcotte (1999), and Hergarten (2002).

2.4.2 The Forest-Fire Model

The forest-fire model is a cellular automaton model that exhibits SOC behavior and mimics the spread of fire in a forest, but is also applied to the spread of biological diseases. We describe the basic model in two dimensions, with a square grid with integer positions $x_{i,j}$.

At every time step a tree (seed) is dropped onto a random location, which corresponds to the planting of a tree if the site is unoccupied. In addition, a match is dropped at a random position every n_s-th time step, so with a "sparking frequency" of $f_s = 1/n_s$. If the site of the dropped match is empty, nothing happens, while a forest fire is started if is occupied by a tree. The spread of the forest fire consumes the tree at the local site and propagates to all adjacent (non-diagonal) neighbor sites, if occupied by a tree. So, the forest fire will spread over a small or large area, depending on the tree density, and will stop once burning finds no further next tree. In the long-term time average, there will be a stable tree density at an intermediate value that is not too small (so that fires cannot spread) and not too high (that would lead to a catastrophic total burn-down). The long-term average tree density will be a critical state that is independent of the initial condition and does not require any fine-tuning of how the initial forest configuration is built up. In several models, a necessary condition for SOC behavior is the double limit of (1) a very low growth probability ($\ll 1$) and (2) an ignition probability much lower than the growth probability. An example of a numerical simulation of this forest-fire model is shown in Fig. 2.11, showing 4 cases from a small fire (with 5 burned trees) to a large forest fire (with over 5,000 burned trees).

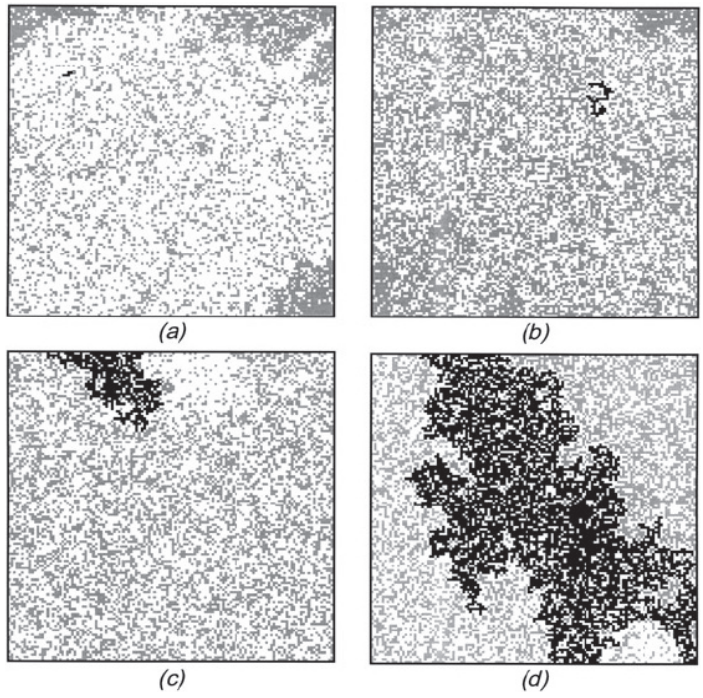

Fig. 2.11 Four examples of typical model forest fires are given for a 128×128 grid with a sparking frequency of $f_s = 1/2{,}000$. The black regions mark the sizes of forest fires, while the grey regions indicate the green (unburned) forest, and white regions correspond to sites without trees. The areas of the 4 forest fires are (a) 5, (b) 51, (c) 505, and (d) 5,327 trees, spanning the entire grid (Turcotte 1999). (Reprinted with permission of the American Physical Society)

In numerical simulations of this forest-fire algorithm, the area A_f of each forest fire is measured and the frequency distributions exhibit powerlaws with slopes in the range of $\alpha \approx 1.0$–1.2 (Turcotte 1999). This is somewhat lower than the observed distribution with a powerlaw of $\alpha \approx 1.3$–1.4 (Section 1.5). The results of three runs are shown in Fig. 2.12. For the smallest sparking frequency ($f_s = 1/2{,}000$), the tree density grows so high in between two forest fires, that the next fire consumes almost the entire forest area (or grid size), which shows up as a peak at the upper limit in Fig. 2.12. This deviation from a straight powerlaw function at the upper end is called a *finite grid size effect*.

Initial numerical simulations of the forest-fire SOC model have been pioneered by Bak et al. (1990), Drossel and Schwabl (1992a,b), Mossner et al. (1992), Henley (1993), and Grassberger (1993). Further model simulations spanned from one to six dimensions (Christensen et al. 1993), were compared with analytical solutions (Drossel et al. 1993), interpreted as a turbulent cascade process (Paczuski and Bak 1993), applied a renormalization group theory (Loreto et al. 1995), or derived scaling laws of critical exponents (Clar et al. 1994). Reviews on the forest-fire model can be found in Mossner et al. (1992), Clar et al. (1996, 1999), Jensen (1998), Hergarten (1998), and Turcotte (1999). Descriptions of forest-fire models can be found in the textbooks of (Jensen 1998, p.65) and Hergarten (1998).

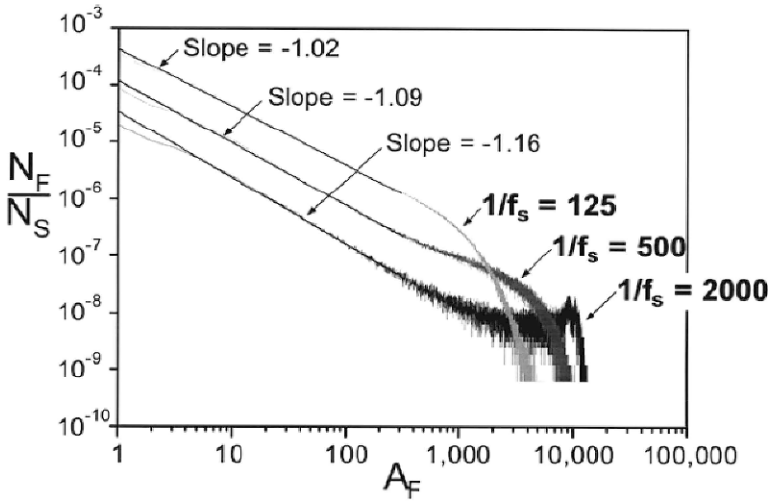

Fig. 2.12 Frequency distributions of forest-fire areas A_f for three different setups, with different sparking frequencies of $f_s = 125$, 500, 2,000. Each run contains $\approx 10^9$ time steps run on a 128×128 grid. The powerlaw slopes are similar (in the range of $\alpha = 1.02$–1.16, but the upper cutoff shows finite grid size effects, approaching the upper limit of the grid $A_F \leq 128^2$ for the smallest sparking frequency (Turcotte 1999). (Reprinted with permission of the American Physical Society)

2.5 SOC Simulations in Magnetospheric Physics

2.5.1 SOC Model with Finite System Size

Some magnetospheric phenomena were found to exhibit powerlaw distributions, such as the burst area of the auroral electro-jet index (AE) or substorm-related tail current disruptions (see observational references in Section 1.6), which seem therefore to be scale-free and consistent with SOC models. On the other side, some other parameters, such as the intensity or time intervals between substorm events seem to have well-defined probability distributions with characteristic scales (see Fig. 1.10). SOC models thus can not explain both statistics, or an additional physical reason may modify the SOC behavior significantly. This dilemma led Chapman et al. (1998) to a dual SOC model where constant energy input (inflow) generates (1) scale-free internal energy discharges with a SOC-like powerlaw behavior, whereas (2) system-wide discharges with a well-defined size distribution do not exhibit SOC. In analogy to the Bak–Tang–Wiesenfeld 2-D sandpile model, the first group of events would include small avalanches confined to the surface of the sandpile that do not reach the base, while the second group would include the largest avalanches that propagate all the way down to the base of the sandpile, where they reach their maximum size, and then would roll over the edge, if the sandpile is mounted on a circular plate (like the IBM experiment with a high-precision scale by Held et al. 1990, see Section 1.2).

Chapman et al. (1998) conducted numerical simulations of such a dual SOC model as follows. A cellular automaton is represented by a 1-D grid of n equally-spaced cells, each one with sand at height h_j and local gradient $z_j = h_j - h_{j-1}$, which is assumed to be stable below a critical angle of repose z. The selection rule for the critical gradients on the n nodes is a random number uniformly distributed in the range $[0,1]$, parameterized by an exponential function for the probability $P(z)$ in the interval $[z, z+dz]$,

$$P(z) = z^y \, \exp\left(\frac{-z^{1+y}}{1+y}\right) , \tag{2.5.1}$$

which has the cumulative probability distribution $F(>z)$

$$F^{cum}(>z) = \int_z^\infty P(z)dz = 1 - \exp\left(-\frac{z^{1+y}}{1+y}\right) , \tag{2.5.2}$$

and the normalization

$$\int_{z=0}^{\infty} P(z)\, dz = P^{cum}(>0) = 1 \, . \tag{2.5.3}$$

Sand is then added at cell 1 at a constant rate $r \ll 1$, until the critical gradient is exceeded at cell 1, triggering a redistribution to neighboring cells until the slope is "flattened" back to the angle of repose ($z_j = 0$). From time to time an avalanche reaches the end of the 1-D grid (at $j = n$), causing a system-wide discharge, in which case the entire sandpile is emptied and returns to the angle of repose. For the statistics of dissipated energies E per avalanche, a nonlinear scaling with a quadratic function is assumed,

$$E = \sum_{j=1}^{n} h_j^2(t_{before}) - \sum_{j=1}^{n} h_j^2(t_{after}) \ , \tag{2.5.4}$$

similar to the model of Dendy and Helander (1997). The quadratic energy scaling can be understood in terms of an area-like spreading for 2-D avalanches, which grows quadratically with the length scale h_j, assuming a constant energy dissipation rate per unit area. Fig. 2.13 (left panel) shows the evolution of dissipated energy as a function of time. Internal avalanches reduce the energy by a partial amount, while system-wide avalanches dump the entire energy of the system to zero, which corresponds to the energy state of the sandpile at the angle of repose. The probability distribution $P(E)$ of the energy dissipated per avalanche exhibits two different components: (1) a powerlaw distribution for internal events, and (2) a peaked distribution for system-wide avalanches (Fig. 2.13, right panel).

This particular set-up mimics the bimodal distribution of magnetospheric substorms (Fig. 1.10) observed by Lui et al. (2000), leading to the interpretation in terms of a nonlinear dissipative system that is driven by a constant inflow, but exhibits scale-free SOC behavior only for internal energy dissipation events, while it exhibits a particular scale for system-wide energy dumps. Such a deviation from a straight powerlaw was also found in system-wide forest-fire events in the simulations shown in (Fig. 2.12), where it was interpreted as a finite-size effect also. Numerical simulations of system-wide avalanches were performed for various (low and high) input rates, in order to mimic the variable loading rates of the magnetosphere, and it was found that the the powerlaw signature of large-scale internal events persisted (Chapman et al. 1999, 2001). Alternatively, a bimodal SOC behavior was also found in a 1-D cellular automaton simulation of the central plasma sheet with two different local instability criteria (Liu et al. 2006).

2.5.2 Cellular Automaton Model with Discretized MHD

SOC behavior in the magnetotail plasma has been inferred early on from the powerlaw distribution of lifetimes found in magnetospheric disturbances based on the auroral electron jet (AE) index (Takalo et al. 1993; Consolini 1997), from near-Earth magnetotail current disruptions (Lui et al. 1988), substorm current disruptions (Consolini and Lui 1999), or bursty bulk flow events (Angelopoulos et al. 1996, 1999). An early attempt to simulate the statistics of these observed features in terms of a cellular automaton SOC model was carried out by Takalo et al. (1999a), as described in the following.

Maxwell's equations in MHD applications generally assume the nonrelativistic limit of plasma motion ($v \ll c$) and are expressed in terms of the current density $\mathbf{j}$ according to Ampère's law (in cgs units),

$$\mathbf{j} = \frac{1}{4\pi}(\nabla \times \mathbf{B}) \ , \tag{2.5.5}$$

yielding together with Ohm's law (with electric conductivity σ) the so-called induction equation,

$$\frac{\partial \mathbf{B}}{\partial t} = \nabla \times (\mathbf{v} \times \mathbf{B}) + \eta \nabla^2 \mathbf{B} \ , \tag{2.5.6}$$

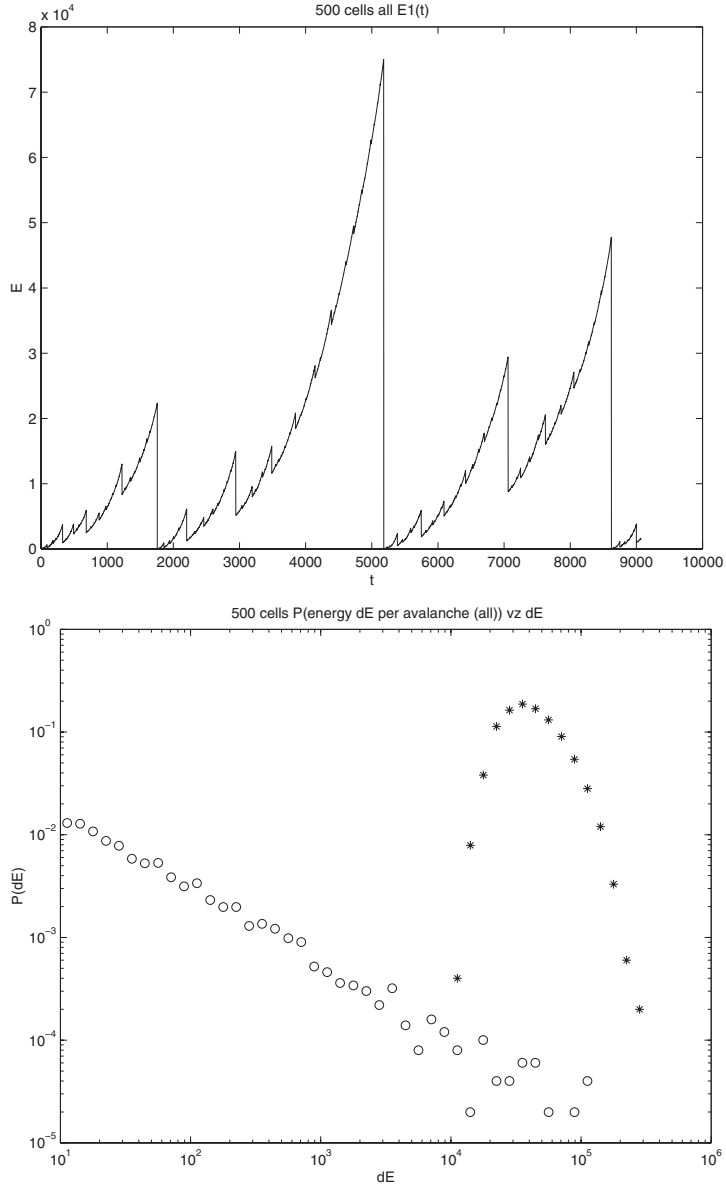

Fig. 2.13 *Left:* Time evolution of a sandpile SOC system with quadratically growing energy and random energy releases. Zero energy corresponds to the energy of the sandpile at the angle of repose. Internal avalanches reduce the total energy to values > 0, while system-wide avalanches drop the energy to values $= 0$. *Right:* A log-log plot of the probability distributions of the energy dissipated for 50,000 internal avalanches (O symbols) and for 10,000 system-wide avalanches ($*$ symbols). Note that the former frequency distribution has a powerlaw shape, while the latter forms a peaked distribution with a peak at $E \approx 10^{4.5}$ (Chapman et al. 1998). (Reprinted with the permission of the American Geophysical Union)

which contains a convective and a magnetic diffusion term (with a magnetic diffusity $\eta = c^2/4\pi\sigma$), and fulfill the divergence-free condition for the magnetic field,

$$\nabla \cdot \mathbf{B} = 0 \,. \tag{2.5.7}$$

Using the vector identity,

$$\nabla \times (\nabla \times \mathbf{B}) = \nabla(\nabla \cdot \mathbf{B}) - (\nabla \cdot \nabla)\mathbf{B} \,, \tag{2.5.8}$$

and Maxwell's equations (Eqs. 2.5.5 and 2.5.7) we have the relation

$$4\pi \, (\nabla \times \mathbf{j}) = -\nabla^2 \mathbf{B} \,. \tag{2.5.9}$$

Making use of Stokes' theorem for a vector field $\mathbf{j}$,

$$\int_S (\nabla \times \mathbf{j}) \cdot \mathbf{n} \, dS \; = \oint_C \mathbf{j} \cdot d\mathbf{l} \tag{2.5.10}$$

we have the relationship,

$$\int \frac{\nabla^2 \mathbf{B}}{4\pi} \cdot \mathbf{n} \cdot d\mathbf{S} = - \oint_C \mathbf{j} \cdot d\mathbf{l} \,. \tag{2.5.11}$$

Applying this functions to a discretized 2-D cellular grid in the xy plane (with cell size $\Delta x = \Delta y$ and area Δx^2) and magnetic field vectors in orthogonal z-direction, $\mathbf{B} = (0, 0, B_z)$, the current density $\mathbf{j}$ has non-zero components only in the xy plane,

$$\mathbf{j} = \frac{1}{4\pi}(\nabla \times \mathbf{B}) = \left(\frac{dB_z}{dy}, -\frac{dB_z}{dx}, 0 \right) = (j_x, j_y, 0) \;, \tag{2.5.12}$$

which can be computed from the the magnetic field $\mathbf{B}(x, y, z)$ at the midpoints $x \pm \frac{1}{2}$ and $y \pm \frac{1}{2}$ between the cell boundaries (Fig. 2.14),

$$j_x \left(x, y \pm \frac{1}{2} \right) = + \frac{1}{4\pi} \frac{dB_z}{dy} = \pm \frac{1}{4\pi} \frac{B_z(x, y \pm 1) - B_z(x, y)}{\Delta y} \;, \tag{2.5.13}$$

$$j_y \left(x \pm \frac{1}{2}, y \right) = - \frac{1}{4\pi} \frac{dB_z}{dx} = \pm \frac{1}{4\pi} \frac{B_z(x, y) - B_z(x \pm 1, y)}{\Delta x} \;. \tag{2.5.14}$$

Summing the currents (j_x, j_y) along the four boundaries of a quadratic cell (Fig. 2.14) leads according to Eq. (2.5.11) to the Laplacian L,

$$\begin{aligned} L \, \Delta x^2 &= \nabla^2 \mathbf{B} \, \Delta x^2 = 4\pi \oint_C \mathbf{j} \cdot d\mathbf{l} \\ &= [j_x(x, y + \tfrac{1}{2}) - j_y(x + \tfrac{1}{2}, y) - j_x(x, y - \tfrac{1}{2}) + j_y(x - \tfrac{1}{2}, y)] \Delta x \\ &= [(B_z(x, y + 1) + B_z(x + 1, y) + B_z(x, y - 1) + B_z(x - 1, y) - 4B_z(x, y)] \;. \end{aligned} \tag{2.5.15}$$

The diffusive term in the induction equation (2.5.6) is then replaced by this Laplacian L, and the conductive term is replaced by a general source term $S(x, y, t)$, representing some

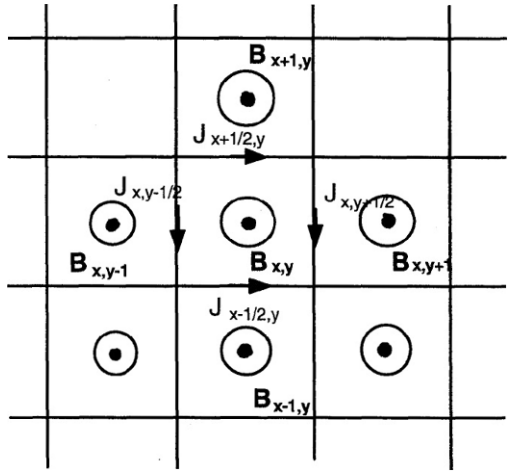

Fig. 2.14 Cellular automaton model containing magnetic fluxtubes, each one characterized by a magnetic field $B_z(x \pm 1, y \pm 1)$ and by four segments of currents $J(x, y \pm \frac{1}{2})$ and $J(x \pm \frac{1}{2}, y)$ at the cell boundaries (Takalo et al. 1999a). (Reprinted with the permission of the American Geophysical Union)

external driving, such as loading of the magnetospheric plasma,

$$\frac{d\mathbf{B}}{dt} = S(x,y,t) + \eta L \, . \tag{2.5.16}$$

The critical threshold level that initiates an avalanche in a cellular automaton model is controlled by the resistivity η of the plasma, which is realized here by a critical Laplacian L_{cr},

$$\eta(x,y) = \eta\,\theta(L - L_{cr}) \, , \tag{2.5.17}$$

where $\theta(...)$ is the Heaviside step function. The Laplacian represents the net current around the cell (x,y). The bigger the resistivity η, the more flux is distributed to neighboring cells during an avalanche. When an avalanche occurs, the excess field,

$$\Delta B = \eta(x,y)(L - L_{cr}) \, , \tag{2.5.18}$$

is evenly redistributed over the next four neighboring cells, one fourth to each of them, similar to the Bak–Tang–Wiesenfeld model (Section 2.1.3). The total energy contained in the magnetic field of the model is then calculated as

$$E(t) = \frac{1}{8\pi} \sum_{x,y=1}^{n} B(x,y,t)^2 \, , \tag{2.5.19}$$

for the cellular grid $(x = 1, ..., n, y = 1, ..., n)$. This 2-D cellular automaton model was run with a grid of $N^2 = 50^2$ cells. The system was continuously driven by a random input with small emerging fields that appear as fluctuations in $B(x,y)$. The evolution of the system in SOC state exhibited frequency distributions of avalanche durations and sizes that are close

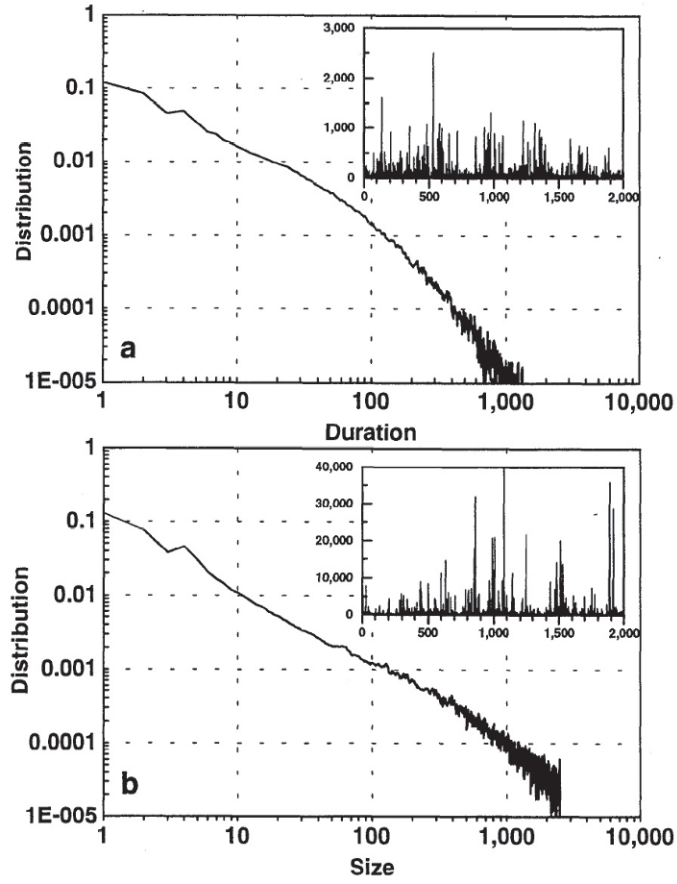

Fig. 2.15 Frequency distributions and time series (inserts) of avalanche durations (top) and sizes (bottom) of 100,000 avalanche events simulated with the cellular automaton model of Takalo et al. (1999a). (Reprinted with the permission of the American Geophysical Union)

to powerlaws at lower values (with a slope of $\alpha \approx 1$), but with a knee at the upper end (Fig. 2.15).

Takalo et al. (1999a) also explored sudden changes of the input, to mimic the southward turning and subsequent northward turning of the interplanetary magnetic field (IMF), by feeding the input of the model with occasional stronger pulses. These intermittent stronger disturbances pushed the model out of the SOC state and triggered larger avalanches during a while, but the system always returned to the SOC state, which demonstrates the robustness of the SOC state. This simulation thus can mimic two different components of magnetospheric substorms: (i) externally triggered substorms caused by perturbations in the solar wind, and (ii) internal substorms caused by the intrinsic dynamics of the magnetosphere near SOC state.

More elaborate numerical simulations of SOC systems with discretized MHD and current-driven kinetic instabilities have been conducted by Klimas et al. (2004), which we will discuss in a selection of physical SOC models (Chapter 9).

2.6 SOC Simulations in Solar Physics

There is a growing industry of SOC avalanche models in solar physics, which is best summarized in the review of Charbonneau et al. (2001). Most SOC models of solar flares are based on the basic idea that a flare is produced by an avalanche of small-scale magnetic reconnection events that cascade in a highly stressed coronal magnetic field, ultimately driven by random photospheric magneto-convection and the solar dynamo.

2.6.1 Isotropic Cellular Automaton Models

Solar flares exhibit a strikingly perfect powerlaw distribution of their peak count rates in hard X-rays, extending over 3–4 orders of magnitude (Fig. 1.13; Dennis 1985). In analogy to the BTW sandpile model, the coronal magnetic field is thought to play the same role of a nonlinear dissipative system in SOC state, where the photospheric convective motion plays the role of the random input of sand grains, the critical angle between misaligned magnetic field lines that leads to magnetic reconnection plays the role of the critical angle of repose in the sandpile, and solar flares play the role of avalanches in SOC state. This interpretation in terms of sandpile SOC systems was first proposed by Lu and Hamilton (1991).

A cellular automaton model was conceived by Lu and Hamilton (1991), where a 3-D grid represents the solar corona, characterized by a magnetic field strength $\mathbf{B_{ij}}$ in each volume element, with a local magnetic field gradient $\Delta\mathbf{B}$ defined by the difference between the local magnetic field and the average of its six nearest neighbors ($\mathbf{B}_{nn}$),

$$\Delta\mathbf{B} = \mathbf{B}_{ij} - \frac{1}{6}\sum_{nn}\mathbf{B}_{nn} \ . \tag{2.6.1}$$

The magnetic field structure is unstable to magnetic reconnection when the difference exceeds a critical field value, $|\Delta\mathbf{B}| > B_c$, similar to the magnetic discontinuity angle proposed by Parker (1988). When a reconnection instability occurs, the redistribution rule is set up in a way that the average magnetic field gradient (Eq. 2.6.1) vanishes, $\Delta\mathbf{B} \mapsto 0$,

$$\mathbf{B}_{ij} \mapsto \mathbf{B}_{ij} - \frac{6}{7}\Delta\mathbf{B} \ , \quad \mathbf{B}_{nn} \mapsto \mathbf{B}_{nn} + \frac{1}{7}\Delta\mathbf{B} \ . \tag{2.6.2}$$

The simulation starts with a uniform magnetic field and is driven by adding random vectors $\delta\mathbf{B}$ at random positions of the field. Once a site gets unstable, the redistribution rule (2.6.2) is applied, the magnetic field gradient is recalculated, and the redistribution rule is applied

iteratively until it becomes stable. Each magnetic reconnection event releases a magnetic energy of

$$E_m = \Delta \sum_k B_k^2 = \left(\frac{6}{7}\right) \Delta \mathbf{B}^2 \ , \tag{2.6.3}$$

where k sums over the unstable cell (i, j) and its next neighbors $(n, n) = (i \pm 1, j \pm 1)$. A new disturbance of the magnetic field is added after the old instability has relaxed.

Note that this redistribution rule is *conservative*, in the sense that the quantity B is conserved after every redistribution step, because the same amount is transferred to the next neighbors that is taken away from the central cell. This conservative property is also genuine to the original sandpile model, where avalanches redistribute sand grains without creating or destroying any. However, although the field quantity B is conserved, the energy B^2 is not conserved after a redistribution step, because of the nonlinear (quadratic) dependence. In fact, every redistribution of $|\Delta B| > B_c$ dissipates energy from the system.

Let us quantify the amount of released energy in every redistribution step more generally for a D-dimensional lattice (e.g., $D = 2$ or 3), with B_{ij} (or B_{nn}) being a scalar variable, and requiring a critical threshold of $|\Delta B| > B_c$ for redistribution. If we denote the new values of the magnetic field with B'_{ij} and B'_{nn}, the average field difference to the next neighbors is then (Eq. 2.6.1),

$$\Delta B = B_{ij} - \frac{1}{2D} \sum_{nn=1}^{2D} B_{nn} \ , \quad |\Delta B| > B_c \ , \tag{2.6.4}$$

and the redistribution rule (2.6.2) reads as

$$B_{ij} \mapsto B'_{ij} = B_{ij} - \frac{2D}{2D+1} \Delta B \ , \tag{2.6.5}$$

$$B_{nn} \mapsto B'_{nn} = B_{nn} + \frac{1}{2D+1} \Delta B \ . \tag{2.6.6}$$

This specific choice of redistribution rule leads to $\Delta B = 0$ after the redistribution, in contrast to the redistribution rules used by Lu et al. (1993). Calculating now the total magnetic energy before (E_m) and after (E'_m) the redistribution step,

$$E_m = B_{ij}^2 + \sum_{nn} B_{nn}^2 \ , \tag{2.6.7}$$

$$E'_m = (B'_{ij})^2 + \sum_{nn} (B'_{nn})^2 \ , \tag{2.6.8}$$

we find the following energy difference, inserting the magnetic field values from Eqs. (2.6.5) and (2.6.6),

$$\begin{aligned} \Delta E &= E'_m - E_m \\ &= \left(B_{ij} - \tfrac{2D}{2D+1}\Delta B\right)^2 + \textstyle\sum_{nn} \left(B_{nn} + \tfrac{1}{2D+1}\Delta B\right)^2 \\ &\quad - B_{ij}^2 - \textstyle\sum_{nn} B_{nn}^2 \\ &= -2B_{ij} \left(\tfrac{2D}{2D+1}\right) \Delta B + \left(\tfrac{2D}{2D+1}\Delta B\right)^2 \\ &\quad + 2 \textstyle\sum_{nn} B_{nn} \left(\tfrac{1}{2D+1}\right) \Delta B + \sum_{nn} \left(\tfrac{1}{2D+1}\right)^2 \Delta B^2 \end{aligned} \ . \tag{2.6.9}$$

From Eq. (2.6.4) we can express

$$\sum_{nn=1}^{2D} B_{nn} = 2D(B_{ij} - \Delta B) \ . \tag{2.6.10}$$

and, together with $\sum_{nn} = 2D$ for summation over constants, inserting into Eq. (2.6.9), we find the final result,

$$\Delta E_m = -\frac{2D}{2D+1}\Delta B^2 \ , \tag{2.6.11}$$

which is the minimum energy quantum that can be released in a redistribution step. This amounts to $\Delta E_m \approx (4/5)\Delta B^2$ for $D = 2$, or $\Delta E_m \approx (6/7)\Delta B^2$ for $D = 3$, respectively, as used in Eq. (2.6.3) by Lu and Hamilton (1991).

A slightly different treatment is given in Charbonneau et al. (2001), where an amount of B_c is redistributed, rather than ΔB,

$$B_{ij} \mapsto B'_{ij} = B_{ij} - \frac{2D}{2D+1}B_c \ , \tag{2.6.12}$$

$$B_{nn} \mapsto B'_{nn} = B_{nn} + \frac{1}{2D+1}B_c \ . \tag{2.6.13}$$

which leads to the following amount for the change of energy (Eq. 5 in Charbonneau et al. 2001),

$$\Delta E_m = -\frac{2D}{2D+1}\left(2\frac{|\Delta B|}{B_c} - 1\right)B_c^2 \ , \tag{2.6.14}$$

but is identical with the result (Eq. 2.6.3 or 2.6.11) of Lu and Hamilton (1991) in the limit of weak driving, i.e., $\Delta B \gtrsim B_c$. In the weak driving limit, only small increments $\delta B \ll B_{ij}$ are added as input to maintain the SOC state. The treatment of Charbonneau et al. (2001) is identical to that of Lu et al. (1993), while the original redistribution rule of Lu and Hamilton (1991) turned out to numerically unstable, as demonstrated by Liu et al. (2002).

A new disturbance of the magnetic field is added after the old instability has relaxed. Lu and Hamilton (1991) find approximate powerlaw distributions for the released energies, i.e., $N(E) \propto E^{-1.4}$, the peak fluxes P, i.e., $N(P) \propto P^{-1.8}$, and the time durations T, similar to those from the observed distributions of hard X-ray flares (Dennis 1985; Crosby et al. 1993),

$$\begin{aligned} N(P) &\propto P^{-1.67\pm0.04} \\ N(E) &\propto E^{-1.53\pm0.02} \\ N(T) &\propto T^{-2.17\pm0.05} \end{aligned} \ , \tag{2.6.15}$$

where the peak energy flux P and total energy E is calculated from the nonthermal spectrum of electrons above a lower cutoff of ≥ 25 keV. The numerically simulated distributions of this SOC model are shown in Fig. 2.16, extending over approximately two orders of magnitude.

The same cellular automaton model for solar flares was repeated for different system sizes, using 3-D grids with length sizes of $L = 10, ..., 50$ (Lu et al. 1993). It was found that the value of the powerlaw slope was invariant to the system size, but the upper cutoffs

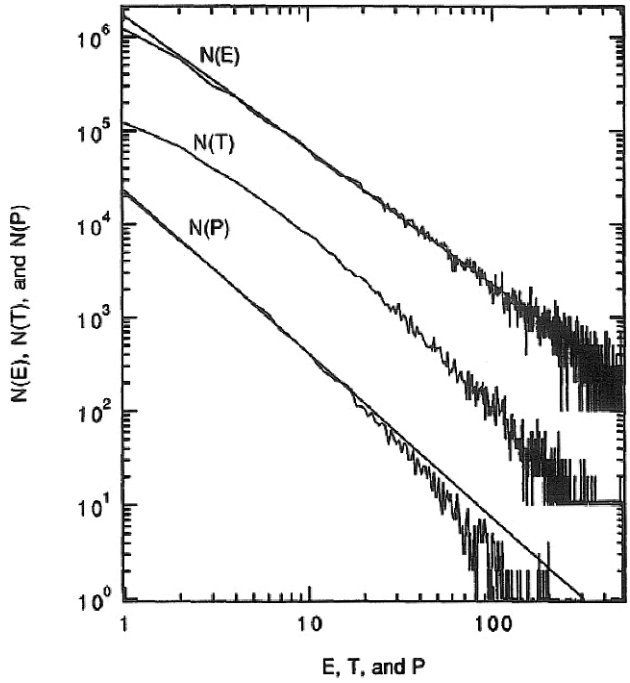

Fig. 2.16 Frequency distributions of event energy release $N(E)$, peak flux $N(P)$, and duration $N(T)$ for avalanches in a $30\times30\times30$ grid according to the SOC model of Lu and Hamilton (1991). The distributions are offset by 1 and 2 orders of magnitude, and slopes of $N(E)\propto E^{-1.4}$ and $N(P)\propto P^{-1.8}$ are indicated with straight lines (reproduced by permission of the AAS).

moved to larger sizes for larger grids, and thus clearly reflect a system-size effect. The rollover at the upper cutoff was found to be close to an exponential function, so that the total distribution can be fitted by

$$N(X)\propto X^{-\alpha}\exp\left(-X/X_c\right)\,, \tag{2.6.16}$$

where X represents (E,P,T) and X_c is the exponential cutoff value. The relationship between the three powerlaw slopes could be explained by a simple physical model of a magnetic reconnection event,

$$\Delta P=\frac{\Delta E}{\Delta T}=\Delta L^2\langle B_\perp^2/8\pi\rangle\frac{v_A}{\zeta}\,, \tag{2.6.17}$$

where v_A is the Alfvén speed and ζ a constant. The relations between the powerlaw slopes of E,P,T reflect correlations that can approximately be quantified by the physical relationship given in Eq. (2.6.15). Scatterplots between these three parameters and the resulting powerlaw distributions fitted to solar hard X-ray flare data from the ISEE-3 spacecraft are shown in Fig. 2.17. We will discuss the functional relationship between powerlaw slopes

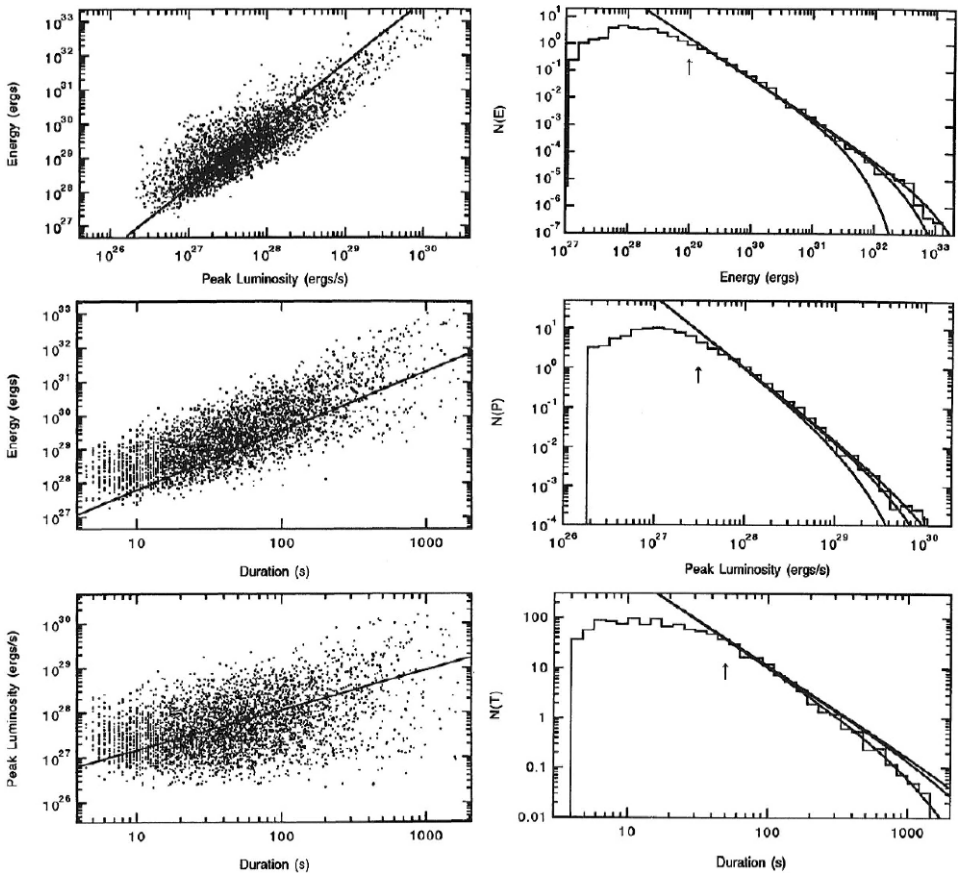

Fig. 2.17 Scatterplots (left) and frequency distributions (right) of the three parameters E (energy), P (peak flux), and D durations of solar flares observed in hard X-rays at energies > 25 keV from ISEE-3. The theoretically predicted correlations (Eq. 2.6.15) are indicated with straight lines (left), and the exponential cutoff function (Eq. 2.6.16) is applied (right) (Lu et al. 1993; reproduced by permission of the AAS).

of frequency distributions and correlations of physical parameters in more detail in Chapter 7. At this point we note that the powerlaw slopes of frequency distributions can be explained by physical relationships that describe the functional dependence between the three parameters E, P, and T. So, it is clearly demonstrated that the powerlaw slope of a specific SOC system is not an universal constant, but depends on the chosen parameters and can be explained by physical laws.

2.6.2 Anisotropic Cellular Automaton Models

In the classic BTW sandpile model, next-neighbor interactions are isotropic, which means that there is an equal probability for the propagation of avalanches or redistribution of

energies in every direction, in 2-D or 3-D lattice models (see Eqs. 2.1.3 and 2.1.4). This isotropic dissipation of energy was also assumed for the magnetic field relaxation in the cellular automaton models first applied to solar flares by Lu and Hamilton (1991) (see Eq. 2.6.2). However, since the solar corona is permeated by magnetic fields, which introduce a preeminent structuring into one-dimensional flux tubes, energy dissipation is not expected to propagate isotropically. Energy release in solar flares is believed to take place in the process of magnetic reconnection, which produces a central current sheet with an X-point that demarcates an ion and electron diffusion region with anisotropic particle transport and energy dissipation. This characteristic of anisotropic energy dissipation was incorporated in 3-D cellular automaton models by defining 6 magnetic field gradients to the next neighbor cells (Vlahos et al. 1995),

$$\begin{aligned}
\Delta B^1_{i,j,k} &= B_{i,j,k} - B_{i+1,j,k} \\
\Delta B^2_{i,j,k} &= B_{i,j,k} - B_{i-1,j,k} \\
\Delta B^3_{i,j,k} &= B_{i,j,k} - B_{i,j-1,k} \\
\Delta B^4_{i,j,k} &= B_{i,j,k} - B_{i,j+1,k} \\
\Delta B^5_{i,j,k} &= B_{i,j,k} - B_{i,j,k-1} \\
\Delta B^6_{i,j,k} &= B_{i,j,k} - B_{i,j,k+1}
\end{aligned} \qquad (2.6.18)\ .$$

instead of one single slope averaged over the 6 next neighbors (Eq. 2.6.1) as introduced by Lu and Hamilton (1991). A redistribution or energy release is then applied when a critical value B_{cr} is exceeded by any of the 6 slopes, say in direction $[i, i+1]$,

$$B_{i,j,k} \mapsto B_{i,j,k} - \frac{6}{7} B_{cr}\ , \quad B_{i+1,j,k} \mapsto B_{i+1,j,k} + \frac{6}{7} B_{cr}\ . \qquad (2.6.19)$$

If more than one direction exceeds the critical threshold B_{cr}, the redistribution of energy is applied to all unstable directions $a \leq 6$, weighted by the relative magnetic field gradient,

$$B_{i\pm1,j\pm1,k\pm1} \mapsto B_{i\pm1,j\pm1,k\pm1} + \frac{6}{7} B_{cr} \frac{\Delta B^a_{i,j,k}}{\sum_a \Delta B^a_{i,j,k}}\ . \qquad (2.6.20)$$

In contrast to the vector field $\mathbf{B}(\mathbf{x})$ used by Lu and Hamilton (1991), a scalar field $B(\mathbf{x})$ is used in Vlahos et al. (1995), which implies that no energy is placed in twisting magnetic fields. Using this anisotropic cellular automaton model, Vlahos et al. (1995) find frequency distributions that are quite different from isotropic cellular automaton models, as shown in Fig. 2.18. The distributions show a plateau with a nearly constant occurrence rate at low energies, and a steep powerlaw cutoff at high energies, with an approximate powerlaw index of $\alpha_E = 3.4 \pm 0.1$ for energies E, $\alpha_P \approx 3.7 \pm 0.1$ for peak luminosities P, and $\alpha_D \approx 8.5 \pm 1.5$ for durations D. It is also found that the extension of the plateau is shorter the lower the critical threshold B_{cr} is set in the numerical simulations. This dual behavior is found to be robust, even when the energy input (i.e., loading by photospheric turbulence) is driven at different rates (Georgoulis and Vlahos 1998).

In a hybrid model, the anisotropic and isotropic model were added together, yielding a synthesized distribution (Fig. 2.19) with a steep powerlaw slope ($\alpha \approx 3.5$) at low energies

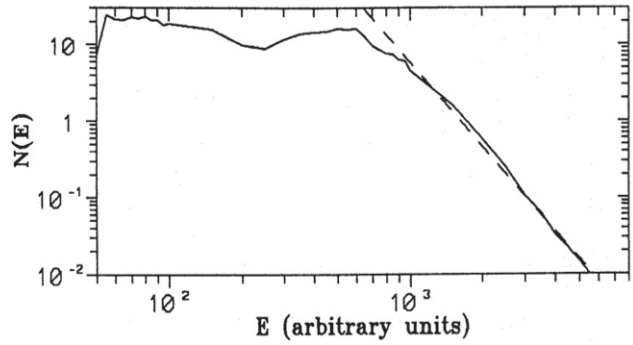

Fig. 2.18 Frequency distribution of energies simulated in a $100 \times 100 \times 100$ grid using a SOC model with anisotropic energy dissipation. The distribution has a flat plateau at low energies and a steep powerlaw slope of $\alpha \approx 3.7$ at high energies (Vlahos et al. 1995).

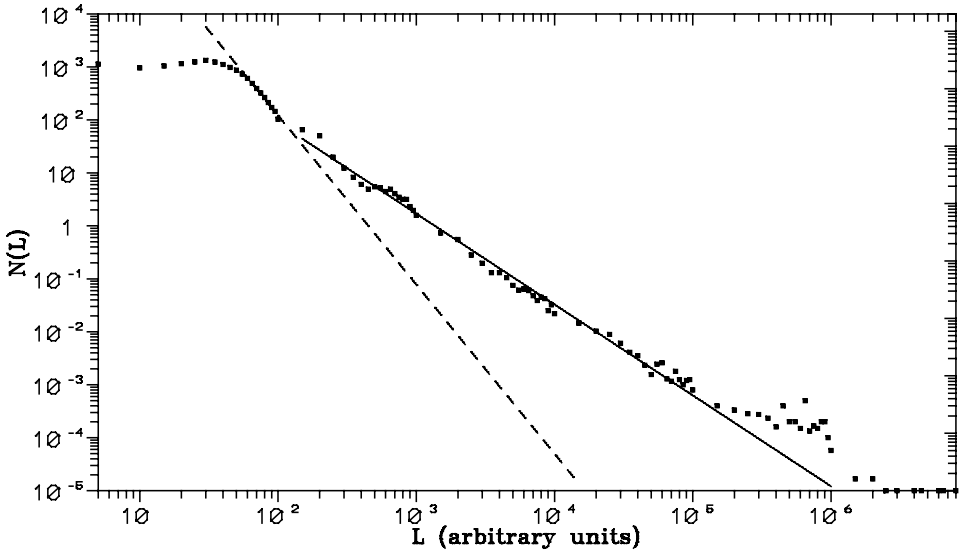

Fig. 2.19 Frequency distribution of the peak luminosity L in a hybrid model with anisotropic energy dissipation for nanoflares and isotropic dissipation for large flares, simulated in a $150 \times 150 \times 150$ grid. The distribution exhibits a steep powerlaw slope of $\alpha \approx 3.3$ at low energies (nanoflares) and a flatter powerlaw slope of $\alpha \approx 1.7$ at high energies for large flares (Georgoulis and Vlahos 1996).

for small flares, and flatter slopes ($\alpha \approx 1.8$) for larger flares (Vlahos et al. 1995; Georgoulis et al. 1995; Georgoulis and Vlahos 1996). This model was also applied to model the bimodal distributions of flare data observed with the WATCH spacecraft (Georgoulis et al. 2001).

This result was interpreted in terms of a unified two-component model of (i) normal flares that release energy in an active region, and (ii) nanoflare events that heat the overall corona. Since the singular value $\alpha = 2$ of the powerlaw slope in energy demarcates

the limit where the integral of the frequency distribution diverges, either at the upper end (for $\alpha < 2$) or lower end (for $\alpha > 2$), the numerical result of the steep slope of nanoflares beyond the critical limit seems to imply that nanoflares could have an unlimited amount of undetected energy available at the lowest energies that could account for coronal heating. However, although some observations suggested a steeper slope for nanoflares (see Fig. 1.14), this result could also be explained by instrumental biases and remained controversial. Sampling nanoflares with comprehensive temperature coverage yielded the same powerlaw slope for nanoflares and large flares (Fig. 1.14), and thus did not support the hybrid model of anisotropic energy dissipation in nanoflares and isotropic dissipation in large flares. However, since anisotropic energy dissipation during magnetic reconnection is more likely based on physical models, it probably applies to both nanoflares and large flares.

2.6.3 Discretized MHD Cellular Automaton Models

The magnetohydrodynamic (MHD) evolution of the coronal or solar flare plasma can be simulated with numerical simulations that solve the ideal or resistive MHD equations, which are based on the basic Maxwell equations known in classical electrodynamics. Such numerical MHD simulations are usually coded in a discretized 2-D or 3-D lattice grid, and thus entail next-neighbor interactions in discretized grids as in the (physics-free) cellular automaton algorithms. So, it is a natural desire to derive a physics-based discretization of the MHD equations in order to understand SOC models in terms of physical models, such as magnetic reconnection that drives solar flares. Some studies have been conducted to derive physics-based cellular automaton models from the discretization of the MHD equations (Vassiliadis et al. 1998; Isliker et al. 1998a, 2000, 2001).

The basic approach of Vassiliadis et al. (1998) has already been described in Section 2.5.2 applied to magnetospheric substorms by Takalo et al. (1999a). Each cell of a 2-D lattice is associated with the cross-section of flux tubes aligned with a magnetic field $\mathbf{B}(x,y) = (0,0,B_z)$ in perpendicular direction (z) to the lattice plane (x,y). The currents $\mathbf{j}(x,y,0) = (j_x, j_y, 0)$ along the four sides of each cell boundary are then computed from the induction equation quantified in terms of discretized magnetic field gradients $(dB/dx, dB/dy)$ between the next-neighbor cells. The induction equation $d\mathbf{B}/dt = \eta\nabla^2\mathbf{B} + S(x,y,t)$, consisting of magnetic diffusion (with magnetic diffusivity constant η) and a convective term, which is represented here with a source term $S(x,y,t)$ that randomly disturbs the magnetic field (like the dropping sand grains on a sandpile), describe the nonlinear dynamics of the system. Magnetic diffusion with classical resistivity η is very slow, and thus nonlinear resistivity $\eta(\mathbf{j})$ is required (for anisotropic cellular automaton models) or hyper-resistivity $\eta(\nabla^2\mathbf{j})$ (for isotropic ones) in order to enable a rapid dissipation and relaxation mechanism (Vassiliadis et al. 1998). The discrete MHD equations satisfy the necessary conditions for a SOC state in terms of local conservation of the magnetic flux and rapid energy dissipation and relaxation by nonlinear resistivity.

Isliker et al. (1988) calculate a discretization of the MHD equation by applying the discrete redistribution rules (Eqs. 2.6.1 and 2.6.2) of Lu and Hamilton (1991) to a 3-D magnetic field and obtain partial differential equations that exhibit a mathematical dis-

continuity at the cell boundaries that is not consistent with the smooth spatial function expected for a magnetic diffusion process.

A new approach was attempted by Isliker et al. (2000), by choosing a vector potential $\mathbf{A}$ as the independent variable to characterize the physical state of each lattice point, instead of using the magnetic field $\mathbf{B}$, which generally does not fulfill Maxwell's equation of a divergence-free field ($\nabla \cdot \mathbf{B} = 0$) when disturbed randomly. The magnetic field is then defined by

$$\mathbf{B} = \nabla \times \mathbf{A} \ , \tag{2.6.21}$$

which automatically fulfills the divergence-free condition,

$$\nabla \cdot \mathbf{B} = \nabla \cdot (\nabla \times \mathbf{A}) = 0 \ . \tag{2.6.22}$$

With this vector potential approach, the redistribution rules (Eqs. 2.6.1 and 2.6.2) of Lu and Hamilton (1991) are then expressed as,

$$\Delta \mathbf{A}_{ij} = \mathbf{A}_{ij} - \frac{1}{6} \sum_{nn} \mathbf{A}_{nn} \ . \tag{2.6.23}$$

$$\mathbf{A}_{ij} \mapsto \mathbf{A}_{ij} - \frac{6}{7} \Delta \mathbf{A}_{ij} \ , \quad \mathbf{A}_{nn} \mapsto \mathbf{A}_{nn} + \frac{1}{7} \Delta \mathbf{A}_{ij} \ . \tag{2.6.24}$$

The changes in the magnetic field variables are then calculated with Eq. (2.6.20), and the current changes with Ampère's Law,

$$\mathbf{j} = \frac{1}{4\pi} (\nabla \times \mathbf{B}) \ . \tag{2.6.25}$$

Having the resulting magnetic field $\mathbf{B}$ defined this way in every cell (x, y, z) and the current densities $\mathbf{j}$ at the cell boundaries $(x \pm \frac{1}{2}, y \pm \frac{1}{2}, z \pm \frac{1}{2})$, the nonlinear system dynamics controlled by the induction equation can then be calculated in the same was as in the approach of Vassiliadis et al. (1998), (see Section 2.5.2 for details). The only difference is that the energy input to the SOC system occurs by random disturbances of the vector potential $\mathbf{A}$, rather than of the magnetic field $\mathbf{B}$. Similar energy distributions are obtained when the energy quantity in each cell is derived from a scalar field $B_k(\mathbf{x})$ or from a vector field $\mathbf{B}(\mathbf{x}) = \nabla \times \mathbf{A}$ (Isliker et al. 2000, 2001). An example of such a simulation is shown in Fig. 2.20, which exhibits similar powerlaw-like frequency distributions as simulated by Lu and Hamilton (1991) or Lu et al. (1993), see Fig. 2.16 and 2.17.

Note that the definition of the released energy based on the square of the magnitude of the vector field as a measure of energy density, i.e. $E \propto \sum B_j^2$ (Eq. 2.6.3) is physically sound when the vector field is assumed to correspond to $\mathbf{B}$, but not for $\mathbf{A}$ (Galsgaard 1996). A modified redistribution rule that removes a constant amount of tension ΔA_{crit}, rather than the full amount of the total field gradient $\Delta A_{i,j,k}$, was suggested by Galsgaard (1996),

$$\mathbf{A}_{i,j,k} \mapsto \mathbf{A}_{i,j,k} - \frac{6}{7} \Delta A_{crit} \frac{\Delta \mathbf{A}_{i,j,k}}{|\Delta \mathbf{A}_{i,j,k}|} \ , \tag{2.6.26}$$

$$\mathbf{A}_{i\pm1,j\pm1,k\pm1} \mapsto \mathbf{A}_{i\pm1,j\pm,k\pm1} + \frac{1}{7} \Delta A_{crit} \frac{\Delta \mathbf{A}_{i,j,k}}{|\Delta \mathbf{A}_{i,j,k}|} \ . \tag{2.6.27}$$

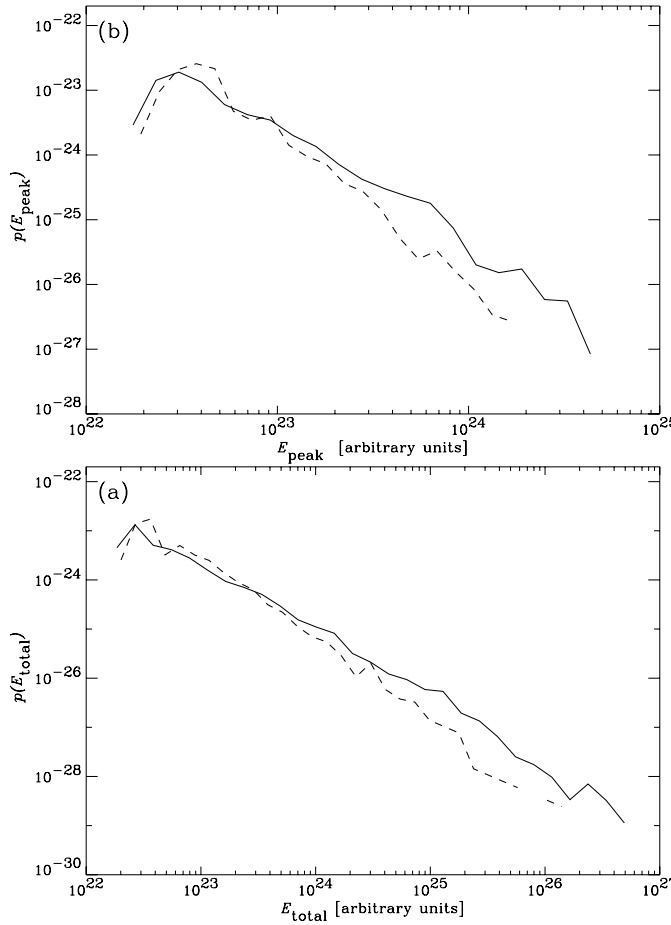

Fig. 2.20 Probability distributions of total energy (top) and peak flux (bottom) of a cellular automaton model that produces current instabilities, mimicking energy releases in solar flares, simulated in terms of discretized MHD equations. The disturbance of the nonlinear system and the threshold for instability is quantified in terms of the vector potential **A** (solid) or current density **j** (dashed) (Isliker et al. 2001).

With some algebra (see Eqs. 2.6.4–2.6.11) it can be shown that the energy released during one redistribution step is (Galsgaard 1996),

$$E_m = \frac{6}{7}\Delta A_{crit}^2 \left(2\frac{|\Delta \mathbf{A}_{i,j,k}|}{\Delta A_{crit}} - 1 \right) , \tag{2.6.28}$$

or more generally for arbitrary dimensions $D = 1, 2, 3, \ldots$ (Charbonneau et al. 2001),

$$E_m = \frac{2D}{2D+1}\Delta A_{crit}^2 \left(2\frac{|\Delta \mathbf{A}_{i,j,k}|}{\Delta A_{crit}} - 1 \right) . \tag{2.6.29}$$

Thus, the smallest "quantum" of energy that can be released by a lattice is (Charbonneau et al. 2001),

$$E_{min} = \frac{2D}{2D+1}\Delta A_{crit}^2 \ . \tag{2.6.30}$$

Comparisons of numerical SOC simulations with full energy redistributions (Lu et al. 1993) and partial energy redistributions (Eqs. 2.6.26–2.6.28) demonstrated that the functional shape of frequency distributions of peak fluxes and energies sensitively depends on the details of the redistribution rules. Galsgaard (1996) found two criteria to be necessary to obtain powerlaw distributions for the energy release: (1) the field must be systematically driven, so that large-scale regions with coherent tension are obtained, and (2) only a fraction of the field quantity triggering the instability must be removed from the local redistribution procedure.

2.6.4 Divergence-Free Field Braiding Models

The solar corona is envisioned to be a system of one-dimensional flux tubes that are subject to a variety of dynamical forces, such as buoyancy forces that make flux tubes emerge from the photosphere and rise into the corona, twisting and braiding caused by photospheric magneto-convection, as well as impulsive pressure forces during magnetic reconnection processes and coronal mass ejections that kick adjacent field lines and cause damped oscillations. The previously considered 2-D or 3-D lattice cellular automaton models capture dynamic processes as time-variable fluctuations of some physical parameters in the coordinate system of a rigid grid, but cannot follow the dynamic motion of an identical magnetic field line or flux tube. A new approach of a cellular automaton model that consists of a lattice grid of deformable magnetic field lines has been developed by Morales and Charbonneau (2008a,b, 2009), similar to the *coronal field braiding model* postulated by Parker (1988). The model, moreover, ensures that the magnetic field stays divergence-free ($\nabla \cdot \mathbf{B} = 0$) during random disturbances, so we call it a "divergence-free field braiding model".

The basic lattice structure of the cellular automaton model of Morales and Charbonneau (2008a) is shown in Fig. 2.21, consisting of initially parallel field lines that have their footpoints rooted in a horizontal 1-D lattice grid (x), while their lengths extend over the vertical axis (y), so that every field line position has a unique coordinate (x,y). This initial setup is periodically disturbed by a random displacement of node (x,y) to position $(x+\Delta x,y)$, which is measured by a misalignment angle $\theta(x,y)$. If the misalignment angle exceeds a critical angle θ_c, the intersecting field lines can reconnect into an alternative configuration by a "cut-and-splice" operation, until a sub-critical misalignment angle is reached. The redistribution rule involves a new connectivity for crossing field lines that has a lower misalignment angle. The example shown in Fig. 2.21 shows a two-step redistribution scheme where field lines 1 and 3 exchange their connectivity in two time steps and end up with a sub-critical angle everywhere. Multiple reconnection steps are often required to reach a new stable state. Such chains of reconnection steps represent the avalanches in sandpiles. Note that the avalanches are highly anisotropic (similar to the models described in Section 2.6.2), in contrast to isotropic avalanches in the BTW sandpile model (Section 2.6.1).

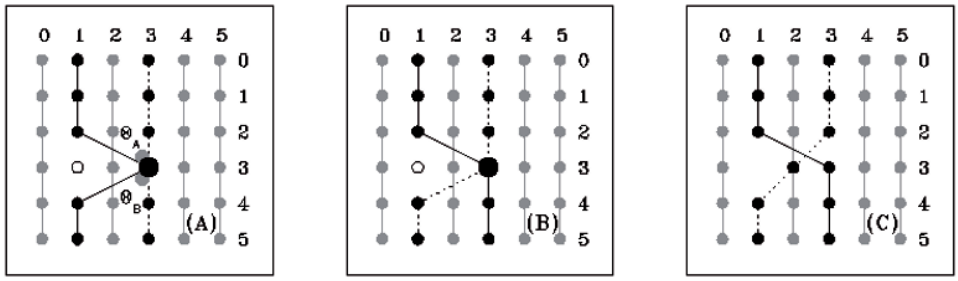

Fig. 2.21 Sequence of a two-step redistribution scheme in the divergence-free field braiding cellular automaton model of Morales and Charbonneau (2008a). Node $j = 3$ of field line $i = 1$ is displaced by two units, causing misalignment angles θ_A and θ_B above a critical value (left frame A), triggering a new connectivity between field line $i = 1$ and $i = 3$ (middle frame B), which is still not stable and triggers another new connectivity between field line 1 and 3 (dashed; right frame C) (reproduced by permission of the AAS).

This braiding model is designed to maintain divergence-freeness during each time step. Initially, every node has a distance Δy to the next neighbor. Let us consider field lines with an initial length of $L = n \times \Delta y$. If a node is displaced by a transverse disturbance of δx in an intermediate position, the new length of the deformed field line is $L' = L - 2\Delta y + 2\sqrt{\Delta y^2 + \delta x^2}$, and the misalignment angle is $\theta = \delta x / \Delta y$. Each field line has a cross-section of $A = \Delta x^2$. In order to ensure mass conservation, the cross-section A' at the deformed location has to reduce (i.e., thinning) to compensate for the stretching of the flux tube mass M,

$$M = \rho A L = \rho A' L' \,, \tag{2.6.31}$$

if we assume a constant density ρ in an incompressible fluid. At the same time, the magnetic flux $\Phi = AB$ has to be conserved

$$\Phi = AB = A'B' \,. \tag{2.6.32}$$

These two conditions yield a scaling of the magnetic field B' with the deformed length L' of the field line,

$$B' = B \left(\frac{L'}{L} \right) \,. \tag{2.6.33}$$

The total magnetic energy of the magnetic field line is then

$$E_m(t) = \frac{1}{8\pi} \int_V \mathbf{B}(t)^2 dV = \frac{V_0}{8\pi} B_0^2 \sum_{i=1}^{n-1} \left(\frac{l_i(t)}{l_0} \right)^2 \tag{2.6.34}$$

where V_0 and B_0 are the initial volume and field strength of a field strand, and $l_i(t)$ is the length of strand i at time t. Every deformation of a flux tube corresponds to a lengthening of $l_i(t)$ and thus represents an energy input into the system. Once the threshold is exceeded, an avalanche of reconnection occurs which shortens the loop segments, corresponding to a decrease or dissipation of the energy according to Eq. (2.6.34). This procedure to vary

the magnetic field strength of a flux strand, in response to stretching its length, conserves the magnetic flux $\Phi = AB$ of a strand by design, and thus the model automatically satisfies the flux conservation constraint or divergence-free condition $\nabla \cdot \mathbf{B} = 0$.

Morales and Charbonneau (2008a) perform numerical simulations with this model and find that the system transitions into a SOC state after an initial stressing phase, where avalanches of all sizes occur and produce powerlaw-like frequency distributions with slopes of $\alpha_E \approx 1.63$–1.72 for energies, $\alpha_P \approx 1.73$–1.84 for peak fluxes, and $\alpha_T \approx 1.79$–1.95 for durations, which are close to the observed values for solar flares (Eq. 2.6.15). This model can be scaled to coronal loops with lengths of $L_0 = 100$ Mm and diameters of $w = 1$ Mm, which yields flare energies in the range of $E_m \approx 10^{23}$–10^{29} erg, for an instability threshold angle of $\theta_{cr} = 11^\circ$, which is similar to the nanoflare model of Parker (1988).

Statistics of avalanche peak areas A with the same model yields powerlaw distributions also,

$$N(A) \propto A^{-\alpha_A} \ , \tag{2.6.35}$$

with a powerlaw slope of $\alpha_A \approx 2.45$ (Morales and Charbonneau 2008b), which indeed also agree with flare areas observed in EUV ($\alpha_A \approx 2.3$–2.7) and soft X-rays ($\alpha_A \approx 1.7$–2.1) (Aschwanden and Parnell 2002). In order to obtain more realistic geometries, the 2-D lattice model was also wrapped onto a cylinder, stretched along the cylinder axis, bent into a semi-circular loop structure, rotated into an arbitrary line-of-sight direction, and projected into the plane of the sky, which mimics an observed image of a flare loop. These transformations changed the frequency distributions of the observed flare areas A slightly, with a powerlaw index of $\alpha_A \approx 2.37$ (Morales and Charbonneau 2009). In addition, the simulated images allow also to determine the fractal Hausdorff dimension D_2,

$$A(L) \propto L^{D_2} \ , \tag{2.6.36}$$

for which a value of $D_2 = 1.17$–1.24 was found (Morales and Charbonneau 2009), which is significantly smaller than the Euclidean limit $D_2 \leq 2$ of solid filling. These simulated values are somewhat lower than observed at the times of peak flux in nanoflares ($D_2 \approx 1.5$–1.9; Aschwanden and Parnell 2002) and in large flares ($D_2 \approx 1.0$–1.9; Aschwanden and Aschwanden 2008a). However, we have to be aware that the fractal structure of observed flare areas generally appears smoothed by insufficient instrumental resolution, temperature discrimination, and background confusion, while numerical simulations produce sharper and crisper images, and thus can measure lower values for the fractal dimension. The inclusion of the fractal dimension in volume modeling affects also energy models of flares, and thus the powerlaw slope of energy frequency distributions (McIntosh and Charbonneau 2001; McIntosh et al. 2002; Mitra-Kraev and Benz 2001; Aschwanden and Parnell 2002). More details about the fractal dimension of SOC structures will be discussed in Chapter 8.

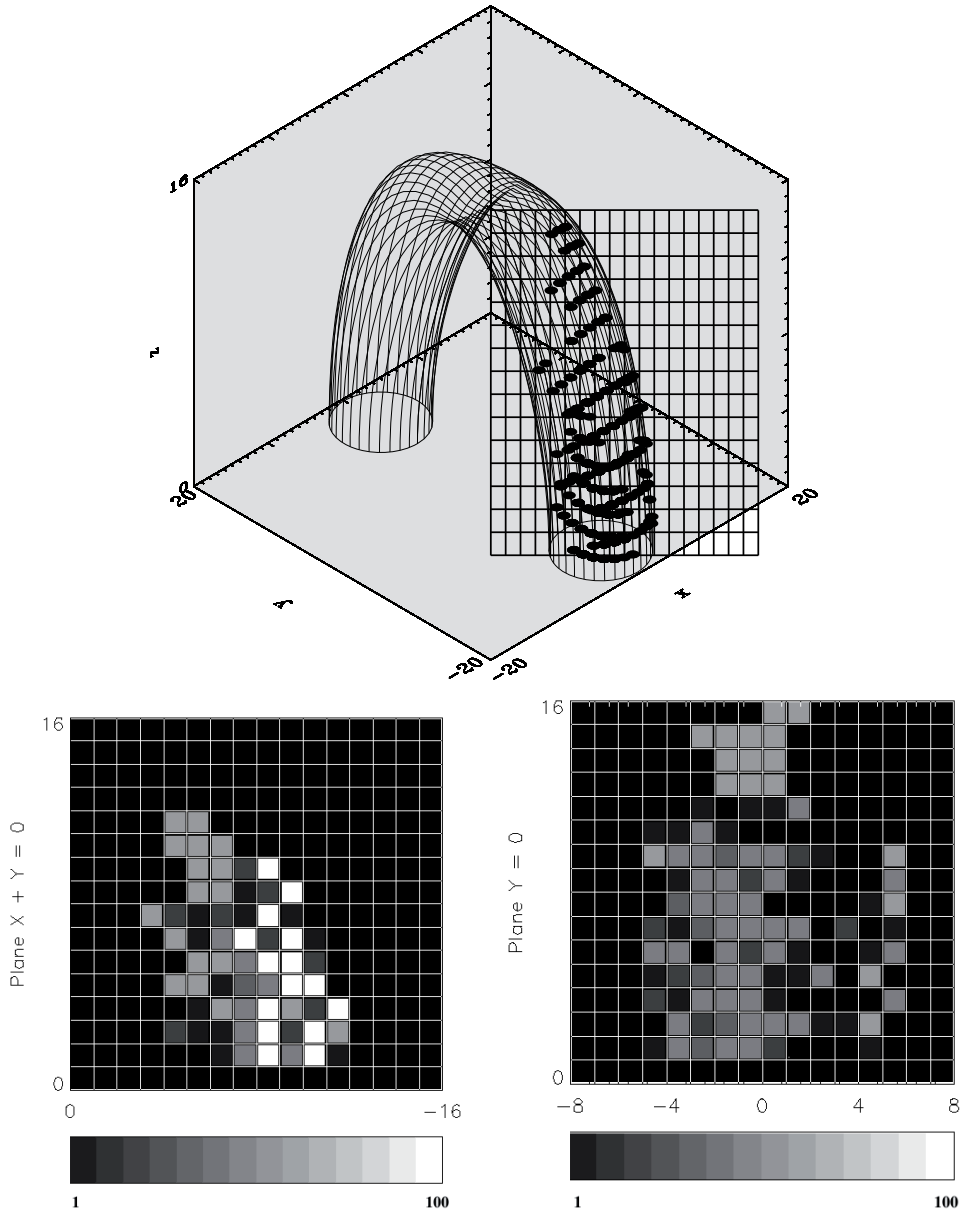

Fig. 2.22 Transformation of the flat 2-D lattice geometry of the divergence-free braiding model onto a pseudo 3-D loop envelope and plane-of-sky for an arbitrary observer's line-of-sight direction (top panel). The fractal area of the projected avalanches are shown for two different directions, for the planes $X+Y=0$ (left) and $Y=0$ (right) (Morales and Charbonneau 2009b; reproduced by permission of the AAS).

2.6.5 Branching Process Models

The previously discussed cellular automaton models all involve a redistribution rule to the next neighbor cells of a lattice grid, which operates whenever a critical threshold is exceeded. A similar concept is a *branching process* in probability theory, which expresses next-neighbor interactions in terms of probabilities.

A simple 1-D cellular automaton model using a branching process applied to solar flares is described in MacKinnon et al. (1996). A lattice site has three states: (1) quiescent, (2) flaring, and (3) flared, so each cell can have three values, $x_i = 0, 1, 2$. The system starts with all sites in state $x_i = 0$. At any time $t = 0, 1, 2, ...$, the i-th site may change from state 0 to state 1 with probability p_0 (representing the driving of the system from outside) if none of its neighboring sites were in state 1 in the previous time step, but with probability $p_1 (> p_0)$ if either of the neighboring sites $i-1$ or $i+1$ were in state 1 in the previous time step, similar to the forest-fire model (Section 2.4.2). Applying these rules iteratively over many time steps leads (by combinational arguments) to the probability distribution $P(n)$ of an event of size n as,

$$P(n) = n p_1^{(n-1)} (1 - p_1)^2 \; . \tag{2.6.37}$$

Averaging these probabilities produces then a size distribution

$$\langle P(n) \rangle = \int_0^1 P(n) dp_1 = \frac{2}{(n+1)(n+2)} \propto n^{-2} \; , \tag{2.6.38}$$

in the limit of $n \mapsto \infty$. Thus, if we associate the size n of an event with the energy E of a flare and the probability $\langle P(n) \rangle$ with the occurrence frequency distribution $N(E)$, this branching process model predicts a size distribution of $N(E) \propto E^{-2}$. Numerical simulations of a branching process with modified rules can produce flatter power law slopes, as demonstrated in Macpherson and MacKinnon (1999).

In an attempt to generalize this 1-D branching process to higher dimensions, Litvinenko (1998a) points out a result from a tree branching process, for which an asymptotic limit was found (Otter 1949),

$$\langle P(n) \rangle \propto n^{-3/2} \exp\left(-\frac{n}{n_0} \right) \; , \tag{2.6.39}$$

which is close to the observed frequency distributions of flare energies.

2.7 SOC Simulations in Astrophysics

The most striking powerlaw distributions observed in astrophysics are the spectra of ultra-high energy cosmic rays that extend over 11 orders of magnitude, or giant pulses from black hole accretion disks, both being the possible result of SOC processes. In the following we summarize a SOC cellular automaton model that has been applied to model the giant pulses from accretion disk systems.

2.7.1 Cellular Automaton Model of Accretion Disk Fluctuations

The X-ray light curves of black-hole candidates, such as Cygnus X-1, were found to have quiescent periods with Planckian power spectra (soft state), as well as active periods with powerlaw-like spectra (hard state), i.e., f^{-p} with $p \approx 1$, which were brought into context of $1/f$-fluctuations or flicker noise of SOC systems (Mineshige et al. 1994a). The rapid variability of X-rays with $1/f$ spectra were discovered not only in black-hole objects, for binary sources, and active galactic nuclei, but also in neutron stars and cataclysmic stars.

Inspired by the BTW model (Bak et al. 1988), the following basic cellular automaton model was set up by Mineshige et al. (1994a). The accretion disk is divided into an outer portion where material smoothly drifts inward, and an inner portion where it suffers an instability and tends to form blobs. Using a 2-D cylindrical coordinate system (r, φ) for the the disk plane (Fig. 2.23), cells are labeled with a radial coordinate $r_i, i = 1, ..., n_i$ and an azimuthal coordinate $\varphi_j, j = 1, ..., n_j$, where r_1 marks the outermost ring of the inner zone. A particle with mass m is put into the outermost cell at r_1. The mass density $M_{i,j}$ is defined as the number of mass particles in cell r_i and φ_j. When the mass $M_{i,j}$ exceeds some critical mass density $M_{crit} \propto r$, a part of the accumulated mass in cell (r_i, φ_j) falls into the 3 adjacent cells of the adjacent inner ring, as a consequence of an unknown instability (such as magnetic reconnection or flares),

$$\begin{aligned} M_{i,j} &\mapsto M_{i,j} - 3m \\ M_{i,j-1} &\mapsto M_{i,j-1} + m \\ M_{i,j} &\mapsto M_{i,j} + m \\ M_{i,j+1} &\mapsto M_{i,j+1} + m \end{aligned} \quad , \tag{2.7.1}$$

After this single redistribution step, further redistributions are executed if one of the newly filled cells exceeds the critical mass M_{crit}, until the whole system is stable again. The

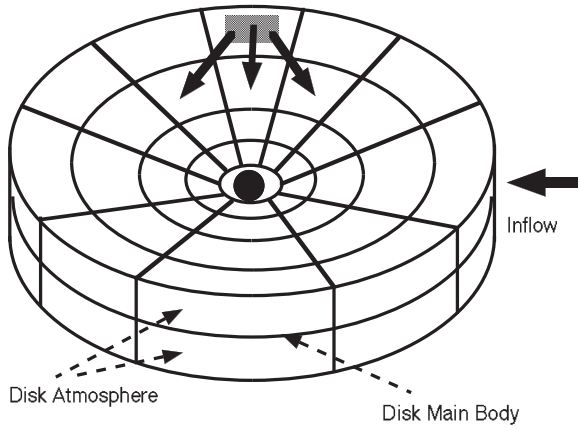

Fig. 2.23 Schematic view of a cellular-automaton model applied to an accretion disk with a black hole in the center. Mass flow from outside randomly triggers avalanches from the outermost ring to inner rings (Yonehara et al. 1997; reproduced by permission of the AAS).

motion of each redistributed k-th particle is tracked from its initial orbit r_i to the final orbit r_j and the the total change in gravitational energy is summed together. The X-ray luminosity L_X resulting from such a mass transfer event is assumed to be approximately proportional to the change in gravitational energy ΔE_{grav},

$$L_X \propto \Delta E_{grav} = GM_{BH}m \sum_k \left(\frac{1}{r_j^k} - \frac{1}{r_i^k} \right) , \tag{2.7.2}$$

where G is Newton's gravitational constant and M_{BH} is the mass of the central black hole. This basic cellular automaton model applies to an accretion disk with rigid rotation. However, a more realistic model should include the effects of differential rotation, which introduces an azimuthal shift j' in the position of the transferred blob, since the orbital time scale in a black-hole accretion disk is much smaller than the blob drift time to an inner radius. Hence, the cellular automaton model should be modified to incorporate this azimuthal shift j' by an amount that corresponds to the differential rotation rate (Mineshige et al. 1994a),

$$\begin{array}{ll} M_{i,j} & \mapsto M_{i,j} - 3m \\ M_{i,j+j'-1} & \mapsto M_{i,j+j'-1} + m \\ M_{i,j+j'} & \mapsto M_{i,j+j'} + m \\ M_{i,j+j'+1} & \mapsto M_{i,j+j'+1} + m \end{array} , \tag{2.7.3}$$

Using this simple cellular automaton model, Mineshige et al. (1994a) are able to produce a powerlaw distribution of energies $N(E) \propto E^{-1.35}$ and a powerlaw distribution of pulse time scales $N(T) \propto T^{-1.7}$, as well as a power spectrum of $S(f) \propto f^{-1.8}$ of the simulated time series, which are all close to the observed values of X-ray pulses from black-hole candidates.

In a slightly modified model, Mineshige et al. (1994b) incorporate a viscous diffusion process, which changes the power spectrum to $S(f) \propto f^{-1.6}$, which is closer to the observed power spectra of $f^{-1.7}$ (Makishima 1988) or $f^{-1.5}$ (Negoro 1992) at $f \gtrsim 1$ Hz. The authors point out that they can obtain different power spectra ($f^{-1.3}$, ..., $f^{-1.1}$) or time scale distributions (from powerlaw-like to exponential) if they change the redistribution rule slightly.

New observations (Negoro et al. 1995) indicated that the peak intensities of X-ray fluctuations from Cygnus X-1 exhibited exponential distributions, rather than powerlaws as expected for SOC, which triggered more modifications of the SOC model in terms of enhancing the effects of gradual diffusion. This model contains additional mass transfer (besides the avalanches specified with Eq. (2.7.3)),

$$\begin{array}{ll} M_{i,j} & \mapsto M_{i,j} - m' \\ M_{i+1,j} & \mapsto M_{i+1,j} + m' \end{array} , \tag{2.7.4}$$

with $m' = m/100,\ m/10,\ m/5$, which flattens the power spectrum and deforms the powerlaw distribution of time scales into exponential distributions (Takeuchi et al. 1995). Further modeling was performed by describing the X-ray fluctuations with fluid dynamics in an advection-dominated disk with critical behavior, which also could reproduce the $1/f$ power spectrum (Takeuchi and Mineshige 1997). More extensions of the model included

relativistic effects, which causes substantial differences if the disk is viewed from directions far from the accretion disk axis (Xiong et al. 2000).

Besides the X-ray fluctuations from X-ray binaries or black-hole accretion disks, which is emitted in an optically thin medium, also the UV radiation from cataclysmic stars (such as Canes Venatici [CV] types), which is emitted from an optically thick medium, was modeled with the same SOC cellular automaton model, which was able to reproduce the observed power spectra that are flat at lower frequencies and have a powerlaw slope of $p \approx 1$–2 at high frequencies (Yonehara et al. 1997).

More advanced SOC cellular automaton models of accretion disks address also the physics of the magnetic field, which entails effects such as the Balbus–Hawley instability (driving a disk dynamo), buoyancy of magnetic fields, magnetic flux emergence, disappearance, and flaring, by including non-local transport of angular momentum in terms of the kinematic viscosity of the magnetic loops in the disk corona (Pavlidou et al. 2001). A snapshot of the magnetic loops in the modeled accretion disk are shown in Fig. 2.24.

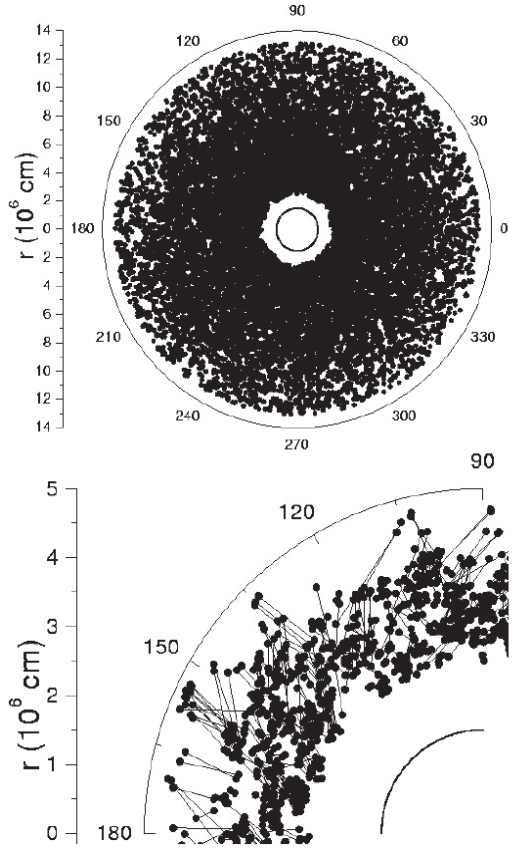

Fig. 2.24 A snapshot of the magnetic loops in a modeled accretion disk surrounding a compact object, shown in full view face-on (top) and as an enlarged segment (bottom), according to simulations with a numerical SOC cellular automaton model by Pavlidou et al. (2001).

2.8 Summary

The theoretical understanding of nonlinear dissipative systems in the state of self-organized criticality started with numerical simulations of a cellular automaton model, which is driven by slow external forcing. The essential framework of a cellular automaton model is a mathematical algorithm that consists of (1) a critical threshold, (2) a next-neighbor redistribution rule that is applied when a local threshold is exceeded, and (3) subsequent iterations of the redistribution rules, until a new equilibrium is reached. Cellular automaton models can simulate the dynamics and outcome of complex multi-element systems, which is often not achievable by analytical theories, but are essentially physics-free models. A great success of cellular automaton models is the reproduction of powerlaw-like distributions for the peak fluxes, energies, and time scales of avalanche events, which emerge as robust characteristics without fine-tuning of the initial conditions. The most influential cellular automaton model in SOC processes is the Bak–Tang–Wiesenfeld (BTW) sandpile model, as well as the slider-block and the forest-fire model in geophysics. After 1990, these cellular automaton models have also been applied in astrophysics, such as in magnetospheric substorms, in solar flares, and in accretion disks, but the meaning of the energy quantity in the BTW sandpile model is often replaced by magnetic energies. Some attempts at reverse engineering have been made to translate the mathematical redistribution rules in SOC sandpile models to physical, discretized differential equations in terms of magneto-hydrodynamics (MHD), which also imply anisotropic transport processes and additional constraints from Maxwell's equations (such as divergence-free magnetic fields). The reduction of physical models of nonlinear processes to discretized cellular automaton algorithms is still in its infancy for astrophysical systems.

2.9 Problems

Problem 2.1: Derive the MHD induction equation (Eq. 2.5.6) from Maxwell's equations and the discretization of the MHD equations outlined in the Eqs. (2.5.5–2.5.19).

Problem 2.2: Derive the amount of released energy in a D-dimensional lattice vector field $\mathbf{A}$ based on the redistribution rule given in Eqs. (2.6.1–2.6.3) and prove the result given in Eqs. (2.6.4–2.6.14).

Problem 2.3: Generalize the divergence-free field braiding model from a 2-D flux tube surface geometry to a 3-D (solidly filled) cylindric geometry. What are the equivalent equations of (2.6.31–2.6.34)?